



Bezier5YS and SHYqp: A general framework for generating data and for modeling symmetric and asymmetric orthotropic yield surfaces

Stefan C. Soare

Technical University of Cluj-Napoca, C. Daicoviciu 15, 40020 Cluj-Napoca, Romania



ARTICLE INFO

Keywords:

Metal plasticity
Constitutive modeling
Quadratic programming
Bezier interpolation
Magnesium alloys

ABSTRACT

The design of conventional yielding criteria, within the phenomenological theory of metal plasticity, is based on a *pointwise* interpolation of experimental data, an approach originating in the early days of plasticity when it was believed that material parameters should be explicitly linked to experimental data. Since the latter is most often a numerical set of a small size, the inherent consequence was that yield functions were, by design, conceived with a small number of parameters as well. For decades, under the constraints of limited computational resources, this approach has had remarkable successes, particularly in the numerical simulation of metal forming operations. However, with the ever increasing level of automation of the assembly lines of most manufacturers, the demand for tight tolerances has pushed the current modeling establishment to its limits. Furthermore, in the current context of climate change, the need for the reduction of energy consumption in the transportation industries has motivated a significant amount of new research into the plasticity of lighter materials such as magnesium alloys. For these, the conventional approach to yield surface modeling has failed to produce adequate models of their yielding and flow properties. This work explores, in the broader framework of data-driven plasticity, a model based on harmonics expansion with data generated by Bezier interpolation. The resulting parameter identification scheme is a quadratic problem with linear constraints (to enforce convexity). It is shown, by applications to magnesium, titanium, aluminum and steel alloys, that the plasticity of virtually any metal can be modeled within this framework with an arbitrary degree of precision. Python code at: <https://github.com/stefanSCS/SHYqp>

1. Motivation

The modeling of the plasticity of metals with asymmetric mechanical properties with respect to the loading direction has been far less successful than that of metals with symmetric properties. The latter have clearly benefited from the inherent simplification brought by symmetry in the mathematical formulation. This simplification is no longer applicable in the case of HCP metals, where the difference between tensile and compression mechanical properties is far from negligible.¹ Hence the mathematical approach to the modeling of yield surfaces has to be substantially reconsidered on more general grounds.

The difficulties posed by the modeling of HCP metals are probably best illustrated by the case of the magnesium alloys AZ31. Traditionally, when dealing with symmetric properties, a model is expected to capture at least the directional properties of the material — the set of yield stresses and r-values: This is a minimal condition for ensuring a basic capability to reproduce deformation patterns and to estimate limit strains. This requirement appears to have been relaxed in some of

the recent articles reporting models of AZ31B: e.g., [Yoon et al. \(2013\)](#) or [Yoon et al. \(2014\)](#), where r-values are not considered at all, most certainly because of the insufficient number of material parameters of the cited models. But even when the underlying yield functions do feature a high number of parameters, and hence allow for the entire set of directional properties to be considered, as in [Plunkett et al. \(2008\)](#) and [Soare and Benzerga \(2016\)](#), the resulting yield surface shapes are remarkably different: The former predicts an egg-shape while the latter a polyhedral. Yet another composite shape, elliptical in tension and polyhedral in compression, is generated by the customized two surface model employed by [Steglich et al. \(2016\)](#) and [Kondori et al. \(2019\)](#).

It is therefore desirable to have a unified, general framework for the design and analysis of models of the yielding and flow properties of metals, with the fundamental property that the modeling error can be decreased in a deterministic fashion when increasing the number of parameters and data. As an alternative to the traditional constitutive

E-mail address: stefancsoare@gmail.com.

¹ For HCP metals there is also the additional problem of evolving mechanical properties. However, once a suitable modeling context is proven for initial or room temperature conditions, its extension to evolving properties is reduced to the task of sequencing with respect to a measure of accumulated plastic deformation.

modeling, a new approach to the problem, inspired by current developments in data science, is gaining momentum — the so-called *data-driven plasticity*. In its purist form, e.g., Ibanez et al. (2016), Eggersmann et al. (2019), this approach bypasses the constitutive model completely, the stress–strain relationship being inferred, or discovered by the computational model (based only on equilibrium and conservation laws) from a large pool of data. More compatible with the current computational infrastructure are data-driven approaches that retain essential constitutive concepts, such as that of yield surface, e.g., Vlassis and Sun (2021), and/or employ a modeling space for the constitutive elements, e.g., Wang et al. (2019), Bomarito et al. (2021), Fuhr et al. (2022). The latter approaches may be regarded as a branch, characterized by support vectors and neural network representations of the yielding surface, of the more established *virtual testing* methodology where crystal plasticity models are employed to generate supplementary data by simulating mechanical tests at macro scale, e.g., Kraska et al. (2009), Zhang et al. (2015), Esmaeili et al. (2019), Roters et al. (2019).

Since yield functions are first order homogeneous, and hence uniquely determined by their values on the unit sphere, the most natural modeling context is that of Fourier series expansions in terms of spherical harmonics.² This was the approach taken by Soare and Benzerga (2016), where Fourier series on the unit circle of the deviatoric subspace were employed to generate isotropic functions that were then used as generators for linear transformations. The linear transformation based approach, however, introduces hard to control non-linearity (in particular, the actual number of independent parameters is practically unknown), turning the procedures of extension to higher precision (by incorporating an arbitrary number of transformations) and parameter identification (by optimization) into tedious tasks. These disadvantages become significant in a context of high precision modeling and far outweigh the benefit of default convexity provided by the linear transformation approach.

In this work we explore a more general scheme, where the analytical expression of the yield function is an amorphous finite sum of harmonic monomials, the latter being selected only on considerations of efficiency and of their ability to change sign with stress reversal. Central to this approach is the data generating procedure. For this purpose we develop a proto-model of the yield surface – Bezier5YS – by interpolating the experimental data based on simple geometrical considerations. While all the theoretical developments take place in the space of 3D stress states, we restrict the range of applications to plane stress conditions for two reasons: (1) The data generating scheme operates in the subspace of plane stresses; (2) The design of general yet tractable 3D formulations, with potential for actual applications, is a significant topic by itself.

2. General framework

The constitutive response of the sheet metal is modeled with respect to a coordinate system aligned along the symmetry axes of the sheet (referred to also as material axes): the x -axis along the rolling direction of the sheet (RD), the y -axis along the transverse direction (TD), and the z -axis perpendicular to the sheet plane (and such that the resulting coordinate system is right-handed); the corresponding unit vectors along the x , y and z -axes are denoted by e_x , e_y and e_z , respectively. For convenience, we shall also use notation with numerical indexes, with the implied correspondence $1 \leftrightarrow x$, $2 \leftrightarrow y$ and $3 \leftrightarrow z$. Thus the orthonormal basis along the xyz -axes will be specified either by e_x , e_y and e_z , or by e_1 , e_2 and e_3 . Summation on repeated (numerical) indices is implied.

² An alternative, in terms of planar Fourier series expansions was proposed by Raemy et al. (2017). However, this approach has to deal with the north-pole singularity of spherical coordinates, and it is not clear how well it extends to 3D stress states.

We shall denote by s the deviatoric component of a stress σ , i.e.,

$$\begin{aligned} s = \sigma - \frac{1}{3} \text{tr}(\sigma) \mathbf{I} = \\ \frac{1}{3}(2\sigma_{xx} - \sigma_{yy} - \sigma_{zz})e_x \otimes e_x + \frac{1}{3}(2\sigma_{yy} - \sigma_{xx} - \sigma_{zz})e_y \otimes e_y \\ + \frac{1}{3}(2\sigma_{zz} - \sigma_{xx} - \sigma_{yy})e_z \otimes e_z \\ + \sigma_{xy}(e_x \otimes e_y + e_y \otimes e_x) + \sigma_{xz}(e_x \otimes e_z + e_z \otimes e_x) \\ + \sigma_{yz}(e_y \otimes e_z + e_z \otimes e_y) \end{aligned} \quad (1)$$

where $\mathbf{I} = e_x \otimes e_x + e_y \otimes e_y + e_z \otimes e_z$ is the identity tensor. The subspace of deviatoric stresses, denoted from now on by \mathbb{S} , is endowed with the natural dot product (in which $e_i \cdot e_j = \delta_{ij}$) and hence with the metric induced by the Euclidean norm (denoted by $| \cdot |$):

$$|s| = \left(s_{xx}^2 + s_{yy}^2 + s_{zz}^2 + 2s_{xy}^2 + 2s_{xz}^2 + 2s_{yz}^2 \right)^{1/2} \quad (2)$$

Modulo a multiplying numerical factor (of $\sqrt{3/2}$), the above norm is simply the formula of the von Mises (isotropic) yield function:

$$|s|^2 = \frac{1}{3} \left[(\sigma_{xx} - \sigma_{yy})^2 + (\sigma_{xx} - \sigma_{zz})^2 + (\sigma_{yy} - \sigma_{zz})^2 + 6\sigma_{xy}^2 + 6\sigma_{xz}^2 + 6\sigma_{yz}^2 \right] \quad (3)$$

In order to define functions with an optimal number of arguments on the deviatoric subspace, an orthonormal basis in \mathbb{S} is constructed as follows (in essence, by a Gram–Schmidt procedure). From the condition $\sigma \cdot \mathbf{I} = 0$, the unit normal to \mathbb{S} is the tensor $\mathbf{n} = (1/\sqrt{3})(e_1 \otimes e_1 + e_2 \otimes e_2 + e_3 \otimes e_3)$. Then the projection of $e_1 \otimes e_1$ on \mathbb{S} is the tensor \mathbf{v}_1 defined by $\mathbf{v}_1 = e_1 \otimes e_1 - [(e_1 \otimes e_1) \cdot \mathbf{n}] \mathbf{n} = (1/3)(2e_1 \otimes e_1 - e_2 \otimes e_2 - e_3 \otimes e_3)$. The first unit basis tensor in \mathbb{S} is chosen to be

$$\mathbf{g}_1 = \mathbf{v}_1 / |\mathbf{v}_1| = \frac{1}{\sqrt{6}} (2e_1 \otimes e_1 - e_2 \otimes e_2 - e_3 \otimes e_3) \quad (4)$$

The second basis vector \mathbf{g}_2 is obtained similarly by first projecting $e_2 \otimes e_2$ on \mathbb{S} to obtain a tensor $\mathbf{v}_2 = (1/3)(-e_1 \otimes e_1 + 2e_2 \otimes e_2 - e_3 \otimes e_3)$. Note that $\mathbf{v}_2 \cdot \mathbf{g}_1 = -1/\sqrt{6} \neq 0$ and hence its orthogonal to \mathbf{g}_1 component is $\mathbf{v}_2^\perp = \mathbf{v}_2 - (\mathbf{v}_2 \cdot \mathbf{g}_1)\mathbf{g}_1 = (1/2)(e_2 \otimes e_2 - e_3 \otimes e_3)$. The second basis tensor is then defined by:

$$\mathbf{g}_2 = \mathbf{v}_2^\perp / |\mathbf{v}_2^\perp| = \frac{1}{\sqrt{2}} (e_2 \otimes e_2 - e_3 \otimes e_3) \quad (5)$$

The rest of the basis vectors in \mathbb{S} are identical to the shear basis tensors in \mathbb{R}^9 (the 9-dim stress space): $e_1 \otimes e_2$, $e_2 \otimes e_1$, $e_1 \otimes e_3$, etc. However, since the stress tensor is symmetric, a contracted representation, in terms of combined shears, such as $e_1 \otimes e_2 + e_2 \otimes e_1$, etc, is much more convenient in practice (where the stress is visualized as a 6-dim object). Then \mathbb{S} is represented as a 5-dimensional vector space with an *orthonormal* basis formed by the two \mathbf{g}_1 and \mathbf{g}_2 defined above, and by

$$\begin{aligned} \mathbf{g}_3 &= \frac{1}{\sqrt{2}} (e_1 \otimes e_2 + e_2 \otimes e_1), \quad \mathbf{g}_4 = \frac{1}{\sqrt{2}} (e_1 \otimes e_3 + e_3 \otimes e_1), \\ \mathbf{g}_5 &= \frac{1}{\sqrt{2}} (e_2 \otimes e_3 + e_3 \otimes e_2) \end{aligned} \quad (6)$$

We denote the components of an element $s \in \mathbb{S}$ with respect to the basis $\{\mathbf{g}_i\}$ by s_i . These are:

$$s_1 = s \cdot \mathbf{g}_1 = \frac{1}{\sqrt{6}} (2\sigma_{11} - \sigma_{22} - \sigma_{33}), \quad s_2 = s \cdot \mathbf{g}_2 = \frac{1}{\sqrt{2}} (\sigma_{22} - \sigma_{33}) \quad (7)$$

$$s_3 = s \cdot \mathbf{g}_3 = \sigma_{12}\sqrt{2}, \quad s_4 = s \cdot \mathbf{g}_4 = \sigma_{13}\sqrt{2}, \quad s_5 = s \cdot \mathbf{g}_5 = \sigma_{23}\sqrt{2} \quad (8)$$

As a verification, one can easily check that for any $s = s_i \mathbf{g}_i$, its norm $|s| = \sqrt{s \cdot s}$ calculated by regarding s as an element of the 5-dim space \mathbb{S} coincides with the Mises formula (3).

Unit tensors in the deviatoric subspace will be generically denoted by \mathbf{u} and the unit sphere of \mathbb{S} by U ; Thus:

$$U = \{\mathbf{u} \mid \mathbf{u} = s / |s|, s \in \mathbb{S}\} \quad (9)$$

In general, the yield functions of metal plasticity are homogeneous³ and pressure independent.⁴ Any such function f is then uniquely characterized by its values on unit tensors:

$$f(\sigma) = f(s) = f\left(|s| \frac{s}{|s|}\right) = |s| f\left(\frac{s}{|s|}\right) = |s| h(u_1, u_2, u_3, u_4, u_5) \quad (10)$$

where $h : U \rightarrow \mathbb{R}^+$ denotes the restriction of f to the unit sphere U of \mathbb{S} .

When the yield function f is isotropic, the function h can be represented as a classical Fourier series expansion. In the general, anisotropic case, the function h can always be expanded into a Fourier series of spherical harmonics

$$h(\mathbf{u}) = c_0 + c_1 \phi_1(\mathbf{u}) + c_2 \phi_2(\mathbf{u}) + c_3 \phi_3(\mathbf{u}) + \dots \quad (11)$$

where the basis functions ϕ_i (the spherical harmonics) are restrictions to the unit sphere U of homogeneous polynomials satisfying the Laplace equation, e.g. Groemer (1996). Detailed developments of such basis functions and of corresponding expansions in a 5-dimensional, orthotropic context will be presented elsewhere. Here, the above equation will serve as a motivation for an initial exploration of the modeling capability and of the possible implementation procedures when particular instances (obtained by truncating to a finite sum of polynomials) of h are considered.

Finally, since two vector bases will be used to represent deviatoric stress states, i.e. $\{e_i \otimes e_j\}$ and $\{g_i\}$, a note on derivatives (gradients) of functions of stress is in order. A function $f : \mathbb{R}^9 \rightarrow \mathbb{R}$, with $f = f(\sigma) = f(\sigma_{ij} e_i \otimes e_j)$, is a regular tensor function with its gradient calculated by the classical formula

$$Df = \frac{\partial f}{\partial \sigma} = \frac{\partial f}{\partial \sigma_{ij}} e_i \otimes e_j \quad (12)$$

When f is pressure independent, the case of interest here, it may be represented also as a function with fewer arguments, of the components of $s = s_i g_i$:

$$f(\sigma) = f(s) = \hat{f}(s_1, s_2, s_3, s_4, s_5) \quad (13)$$

The relationship between the partial derivatives of the two representations is obtained by observing that the two functions are actually defined on the same domain (\mathbb{S}) and hence, in tensor form, $Df = D\hat{f}$, that is:

$$\frac{\partial f}{\partial \sigma_{ij}} e_i \otimes e_j = \frac{\partial \hat{f}}{\partial s_k} g_k \quad (14)$$

After expanding the right-hand member using the formulas in Eqs. (4)–(6), identifying the components on the $e_i \otimes e_j$ basis elements obtains:

$$\begin{aligned} \frac{\partial f}{\partial \sigma_{11}} &= \sqrt{\frac{2}{3}} \frac{\partial \hat{f}}{\partial s_1}, \quad \frac{\partial f}{\partial \sigma_{22}} = \frac{1}{\sqrt{2}} \frac{\partial \hat{f}}{\partial s_2} - \frac{1}{\sqrt{6}} \frac{\partial \hat{f}}{\partial s_1}, \\ \frac{\partial f}{\partial \sigma_{33}} &= -\left(\frac{1}{\sqrt{6}} \frac{\partial \hat{f}}{\partial s_1} + \frac{1}{\sqrt{2}} \frac{\partial \hat{f}}{\partial s_2} \right) \end{aligned} \quad (15)$$

³ The primary constitutive element in metal plasticity is, in fact, the elastic domain — the set of all stresses that can be attained at a material point by pure elastic deformation with respect to the current configuration. Experiments show that, within non-damaging stressing limits, every proportional loading/unloading path maintains the same elastic slope, and hence the elastic domain is star-shaped with respect to its center. Any such set can be uniquely described as the level set of a corresponding homogeneous function. Furthermore, non-homogeneous functions can have level-sets that split into several non-connected subsets, a non-desirable feature.

⁴ Ductile damage – pores – effects are not considered here. On the other hand, the yielding of metals does feature a certain intrinsic pressure dependence, Spitzig and Richmond (1984), manifested at crystal lattice level. However, for most metals of interest, the magnitude of this dependence is small and its manifestation at macroscopic level is linear, leaving unchanged the yielding and flow rule in the subspace of deviatoric stresses, Soare and Barlat (2014).

$$\frac{\partial f}{\partial \sigma_{12}} = \frac{1}{\sqrt{2}} \frac{\partial \hat{f}}{\partial s_3}, \quad \frac{\partial f}{\partial \sigma_{13}} = \frac{1}{\sqrt{2}} \frac{\partial \hat{f}}{\partial s_4}, \quad \frac{\partial f}{\partial \sigma_{23}} = \frac{1}{\sqrt{2}} \frac{\partial \hat{f}}{\partial s_5} \quad (16)$$

3. A specific representation: SHYqp

The rapidity with which a Fourier series expansion of a function h converges depends on the smoothness of h and on the complexity of its level sets. In general, however, even for relatively simple shapes of the elastic domain the number of terms required for their modeling is relatively high by comparison with conventional yield functions. In this work we use simple monomial basis functions and consider the following particular form of Eq. (10)

$$f(\sigma) = \sqrt{3/2} |s| h(u) = \sqrt{3/2} |s| [1 + P(\mathbf{u}) + Q(\mathbf{u})] \quad (17)$$

where

$$P(\mathbf{u}) = \sum_{i=0}^{N_P} c_{Pi} \phi_{Pi}(\mathbf{u}), \quad Q(\mathbf{u}) = \sum_{j=0}^{N_Q} c_{Qj} \phi_{Qj}(\mathbf{u}) \quad (18)$$

with the basis functions described by

$$\phi_{Pi}(\mathbf{u}) = u_1^{k_{i1}} u_2^{k_{i2}} u_3^{2k_{i3}}, \quad k_{i1} + k_{i2} + 2k_{i3} = n_P \quad (19)$$

$$\phi_{Qj}(\mathbf{u}) = u_1^{k_{j1}} u_2^{k_{j2}} u_3^{2k_{j3}}, \quad k_{j1} + k_{j2} + 2k_{j3} = n_Q \quad (20)$$

Thus P and Q are orthotropic homogeneous polynomials in the components (u_1, u_2, u_3) , of degrees n_P and n_Q , respectively. We note that the normal stress component σ_{zz} is automatically incorporated in the above expressions.

P and Q are restrictions to the unit sphere of \mathbb{S} of the corresponding polynomials, that is, they can also be regarded as functions defined over \mathbb{S} , of arguments (s_1, s_2, s_3) . As shown later in this article, this has significant implications when calculating the gradient and the hessian. We use monomials instead of trigonometric expressions because the latter require special treatment at the north pole of a spherical coordinate map, where the map is singular. The homogeneity degrees are subject to

$$n_Q = 2m, \quad n_P = 2m-1, \quad m \geq 2 \quad (21)$$

In particular, Q is even and P is odd. The role of the multiplying factor $\sqrt{3/2}$ is to reduce the yield criterion to the Von Mises yield function when $P(\mathbf{u}) \equiv 0$ and $Q(\mathbf{u}) \equiv 0$. A complete expansion as in (10) would use all the lower terms up to P and Q . We dropped all these lower terms, with the exception of the constant term, on grounds of computational efficiency (at the expense of losing some modeling power).

The parameters of the model are the coefficients c_{Pi} and c_{Qj} . Based on Eqs. (19), (20) and (21), the number of coefficients of P and Q are, respectively:

$$N_P(m) = (2m-1+1) + (2m-1-2+1) + \dots + 2 = m(m+1) \quad (22)$$

$$N_Q(m) = (2m+1) + (2m-2+1) + \dots + 1 = (m+1)^2 \quad (23)$$

The specific combination of P and Q in Eq. (17) will be referred to as SHYqp.⁵ Thus the total number of parameters of SHYqp is $N_P + N_Q = (m+1)(2m+1)$. While m can be arbitrarily large in theory, an actual numerical implementation has to consider the finite precision used by computers to represent numbers as well as the overall computational time. The degree of Q in the Python code provided is limited to $n_Q \leq 24$, i.e., $m \leq 12$. Thus the maximum allowed number of parameters in the numerical implementation of SHYqp is 351.

⁵ “SHY” conveniently abbreviates “spherical harmonics yield”.

To illustrate Eq. (17), we unfold here the simplest (nontrivial) case when $n_Q = 4$:

$$P = c_3^1 u_3^3 + c_3^2 u_1^2 u_2 + c_3^3 u_1 u_2^2 + c_3^4 u_2^3 + (c_3^5 u_1 + c_3^6 u_2) u_3^2 \quad (24)$$

$$Q = c_4^1 u_1^4 + c_4^2 u_1^3 u_2 + c_4^3 u_1^2 u_2^2 + c_4^4 u_1 u_2^3 + c_4^5 u_2^4 + (c_4^6 u_1^2 + c_4^7 u_1 u_2 + c_4^8 u_2^2) u_3^2 + c_4^9 u_3^4 \quad (25)$$

where the coefficients c_3^i and c_4^j are the parameters of the polynomials P and Q , respectively. Then the most general extension of SHYqp for $n_Q = 4$ to 3D stress states reads

$$P = c_3^1 u_3^3 + c_3^2 u_1^2 u_2 + c_3^3 u_1 u_2^2 + c_3^4 u_2^3 + (c_3^5 u_1 + c_3^6 u_2) u_3^2 + (c_3^7 u_1 + c_3^8 u_2) u_4^2 + (c_3^9 u_1 + c_3^{10} u_2) u_5^2 + c_3^{11} u_3 u_4 u_5 \quad (26)$$

$$\begin{aligned} Q = & c_4^1 u_1^4 + c_4^2 u_1^3 u_2 + c_4^3 u_1^2 u_2^2 + c_4^4 u_1 u_2^3 + c_4^5 u_2^4 \\ & + (c_4^6 u_1^2 + c_4^7 u_1 u_2 + c_4^8 u_2^2) u_3^2 + c_4^9 u_3^4 + \\ & (c_4^{10} u_1^2 + c_4^{11} u_1 u_2 + c_4^{12} u_2^2) u_4^2 + c_4^{13} u_4^4 \\ & + (c_4^{14} u_1^2 + c_4^{15} u_1 u_2 + c_4^{16} u_2^2) u_5^2 + c_4^{17} u_5^4 + \\ & c_4^{18} u_3^2 u_4^2 + c_4^{19} u_3^2 u_5^2 + c_4^{20} u_4^2 u_5^2 + (c_4^{21} u_1 + c_4^{22} u_2) u_3 u_4 u_5 \end{aligned} \quad (27)$$

amounting to a total of 33 parameters c_3^i and c_4^j . We do not consider this type of extension here since our data generating scheme is reduced to plane stress states. Let us note also that once a *convex* expression in Eq. (17) is identified, one can instantly obtain a convex extension to 3D stress states by substituting u_3 with the linear combination $u_3 + u_4 + u_5$. This has the advantage that uses only the plane stress parameters, at the expense of accepting an overall monoclinic symmetry.

4. Constructing a Bezier proto-model and generating data

The most common experimental characterization of the yielding and flow properties of sheet metal encountered in practice is limited to uniaxial tensile/compression tests on samples cut from the sheet at angles 0°, 45° and 90° from RD. Balanced biaxial tests are rare, but one can infer with some approximation the yielding and r-values at these stress points. Thus, overall, when modeling plastic properties with tension-compression asymmetry, about 16 data points are usually available. Obviously, from a pointwise perspective, the number of data points is far less than the potentially large number of parameters featured by SHYqp. A data generating scheme has to be used in order to fill the gap. Usually this scheme is based on crystal plasticity simulations but here we adopt a simpler scheme based explicitly on the available data. This section introduces a new approach for generating a proto-model of the plane stress yielding surface based on Bezier interpolation — the conceivably ideal blueprint of the yielding surface. This proto-model, referred to as Bezier5YS, is a yield surface model by itself and its complete operational details will be presented elsewhere. Here we are only interested in its data generating capabilities.

Bezier interpolation was first used in yield surface modeling by Vegter et al. (1995) and further refined in Vegter and Boogaard (2006). The approach taken here differs significantly from that of Vegter and his coworkers in two essential aspects:

- It enforces C^2 smoothness (while Vegter's approach enforces C^1 smoothness only)
- It operates on the stress space ($\sigma_{xx}, \sigma_{yy}, \sigma_{xy}$) (while Vegter's operates on principal stresses)

By enforcing C^2 smoothness we gain additional control over the shape of the yield surface. Working in stress space allows us to use explicitly the geometry contained within the experimental data and instantly generate the corresponding yield surface. Recently, Hao and Dong (2020) also attempted a direct modeling in the 3D stress space ($\sigma_{xx}, \sigma_{yy}, \sigma_{xy}$) based on Bezier interpolation. However, their method of constructing

the yield surface relies on a particular ‘longitude’-‘latitude’ mesh which employs several unnatural assumptions: inference of data from other yield functions, different approaches for the symmetric and asymmetric cases, the exterior normals at the balanced biaxial points are assumed to be the same for tension and compression, a mix of interpolation degrees. By contrast, the interpolation scheme presented here uses input only from data, works the same for symmetric and asymmetric yield surfaces, and makes no assumptions other than the basic geometrical requirements that are normally employed for the construction of any smooth curve; In addition, it provides a minimal consistency check of the data: the algorithm can detect if the data-set is not compatible with a convex shape.

In general, no experimental data on second order derivatives is available and hence we have to resort to a particular form of interpolant, described in what follows. Here, all considerations are for plane curves. The Bezier interpolant, chosen based on the requirements that it can be inserted in any assembly (patch) with C^2 -contact at its end points and that its shape can be controlled via a shape parameter, is defined by:

$$\gamma(t) := \sum_{i=0}^5 \phi_i(t) B_i \quad (28)$$

with the coefficient functions ϕ_i , the Bernstein polynomials of order 5, defined, for $t \in [0, 1]$, by

$$\phi_i(t) := C_5^i t^i (1-t)^{5-i}, \text{ with } C_5^i := \frac{5!}{i!(5-i)!}$$

The control polygon $\{B_0, B_1, B_2, B_3, B_4, B_5\}$ is defined by the two endpoints $B_0 = B_S$ and $B_5 = B_E$, the unit tangent directions at the start and end points, μ_S and μ_E , respectively, and by:

$$B_1 := B_S + \lambda_S \mu_S, \quad B_2 := B_1 + (B_1 - B_0) = B_S + 2\lambda_S \mu_S \quad (29)$$

$$B_4 := B_E - \lambda_E \mu_E, \quad B_3 := B_4 + (B_4 - B_5) = B_E - 2\lambda_E \mu_E \quad (30)$$

with $\lambda_S, \lambda_E \in \mathbb{R}$ the *shape parameters* of the Bezier curve. This particular control polygon has the properties: $\gamma(0) = B_S$, $\dot{\gamma}(0) = 5\lambda_S \mu_S$, $\ddot{\gamma}(0) = \mathbf{0}$, $\gamma(1) = B_E$, $\dot{\gamma}(1) = 5\lambda_E \mu_E$, $\ddot{\gamma}(1) = \mathbf{0}$. From now on, any such Bezier curve $\gamma = \gamma(t)$ will be identified by its set of parameters:

$$\gamma = \{B_S, \mu_S, B_E, \mu_E, \lambda_S, \lambda_E\} \quad (31)$$

Patches of several Bezier curve segments will be employed to interpolate the uniaxial data and to construct plane stress yield surface models in 3D space. Two Bezier segments

$$\gamma_1 = \{B_{1S}, \mu_{1S}, B_{1E}, \mu_{1E}, \lambda_{1S}, \lambda_{1E}\} \text{ and}$$

$$\gamma_2 = \{B_{2S}, \mu_{2S}, B_{2E}, \mu_{2E}, \lambda_{2S}, \lambda_{2E}\}$$

are C^2 connected at $B_{1E} = B_{2S}$ if and only if $\mu_{1E} = \mu_{2S}$ and $\lambda_{1E} = \lambda_{2S}$.

• Bezier interpolation of directional data

For a set of uniaxial loading mechanical tests performed at a discrete set of angles

$$\{\theta_{Tk} \in [0, \pi/2] \mid k = 0, \dots, N_T\} \text{ and } \{\theta_{Ck} \in [0, \pi/2] \mid k = 0, \dots, N_C\}$$

from the RD, the resulting experimental data may consist of two pairs of data sets, the directional yield stresses and r-values in tension and compression, $\{\sigma_{T\theta_{Tk}} \mid k = 0, \dots, N_T\}$ and $\{\sigma_{C\theta_{Ck}} \mid k = 0, \dots, N_C\}$, $\{r_{T\theta_{Tk}} \mid k = 0, \dots, N_T\}$ and $\{r_{C\theta_{Ck}} \mid k = 0, \dots, N_C\}$, respectively. Here $N_T + 1$ and $N_C + 1$ denote the total number of sampling directions in tension and compression, and the subscripts 'T' and 'C' are used to indicate tension and compression, respectively.

This experimental data set is to be interpolated with Bezier patches as defined above but with an additional assumption: The shape parameters are all equal. This assumption reduces the range of variation of the interpolated data to a more manageable set of functions. Since only the slopes at the two ends $\theta = 0$ and $\theta = 90^\circ$ are known (orthotropic symmetry requires that both end slopes be zero), the rest of the tangent

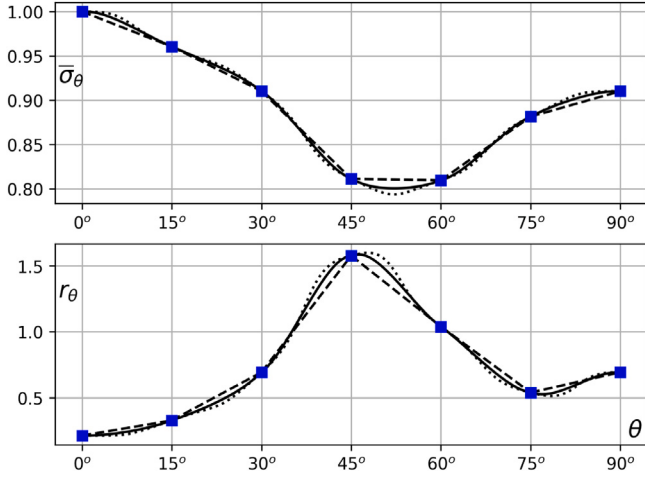


Fig. 1. Plot of several Bezier5YS interpolated directional properties of AA-2090T3: dashed, continuous and dotted corresponding to shape parameters $\lambda = s\lambda_{MAX}$ for scaling $s = 0.0, 0.6$ and 1.0 , respectively (the averaging parameter for tangents in Eq. (32) was set to $\mu = 0.5$ for all three cases).

directions will be inferred from the data as follow. Letting $P_1(x_1, y_1)$, $P_2(x_2, y_2)$ and $P_3(x_3, y_3)$ denote three consecutive data points in the plane (θ, σ) , or in the plane (θ, r) , a tangent vector at P_2 is estimated as:

$$\nu := (1 - \mu)(P_2 - P_1) + \mu(P_3 - P_2) \quad (32)$$

with $\mu \in [0, 1]$ the averaging parameter. Since P_i are equally spaced along the x -axis it follows that:

$$v_x = (1 - \mu)(x_2 - x_1) + \mu(x_3 - x_2) = \Delta x$$

where $\Delta x := x_{i+1} - x_i$ is the grid step along the θ -axis. The unit tangent at an inner data point P_i is then defined by:

$$\tau := \nu / |\nu|, \text{ with: } v_x = \Delta x, v_y = (1 - \mu)(y_i - y_{i-1}) + \mu(y_{i+1} - y_i) \quad (33)$$

The shape parameter $\lambda \geq 0$ can take any value up to a consistency limit: within each Bezier segment of the patch the control points B_2 and B_3 must satisfy $B_{2x} \leq B_{3x}$. This implies the following bounds on λ :

$$0 \leq \lambda \leq \lambda_{MAX} := \text{Min} \left\{ \frac{\Delta\theta}{2(t_{kx} + t_{(k+1)x})} \mid k \geq 1 \right\} \quad (34)$$

An illustration of the effect the shape parameter λ has on the Bezier interpolation of directional data is shown in Fig. 1 where: the dashed line (corresponding to $\lambda = 0$) is basically a polygonal line through the data points, while the dotted line (corresponding to $\lambda = \lambda_{MAX}$) has the highest curvature.

• Bezier interpolation of plane sections

Having interpolated on the interval $0 \leq \theta \leq \pi/2$ the directional uniaxial data for the yielding stresses in tension and compression with smooth functions $\bar{\sigma}_T(\theta)$ and $\bar{\sigma}_C(\theta)$, respectively, the actual corresponding curves on the yield surface are:

$$\gamma_T(\theta) = \bar{\sigma}_T(\theta) (\cos^2 \theta, \sin^2 \theta, \sin \theta \cos \theta) \quad (35)$$

$$\gamma_T^s(\theta) = \bar{\sigma}_T(\pi/2 - \theta) (\sin^2 \theta, \cos^2 \theta, -\sin \theta \cos \theta) \quad (36)$$

$$\gamma_C(\theta) = \bar{\sigma}_C(\theta) (-\cos^2 \theta, -\sin^2 \theta, -\sin \theta \cos \theta) \quad (37)$$

$$\gamma_C^s(\theta) = \bar{\sigma}_C(\pi/2 - \theta) (-\sin^2 \theta, -\cos^2 \theta, \sin \theta \cos \theta) \quad (38)$$

where, because of the assumed orthotropic symmetry, γ_T is above the $\sigma_{xy} = 0$ plane and γ_T^s is the mirror image of γ_T below the plane

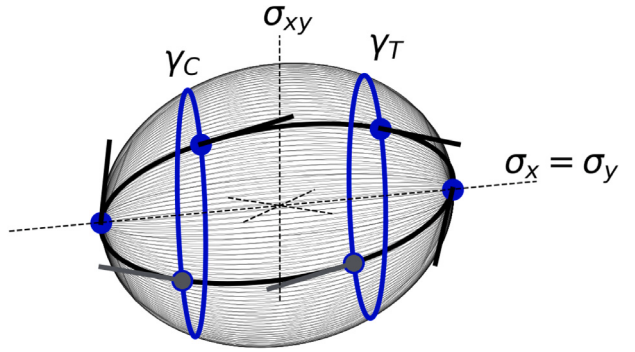


Fig. 2. Construction of the Bezier5YS proto-model: The two blue curves represent the uniaxial tension and compression curves γ_T and γ_C , respectively; A $\Pi(\theta)$ -plane section through the yield surface, represented here with thick black line, is constructed by using the four intersection points of $\Pi(\theta)$ with γ_T and γ_C , the two balanced-biaxial points, and the corresponding tangents. (For interpretation of the references to color in this figure legend, the reader is referred to the web version of this article.)

$\sigma_{xy} = 0$, with a similar positioning holding for the symmetric pair of compression curves γ_C and γ_C^s . Also, in order to preserve the continuity of the tangents along the closed loop formed by a top-bottom pair, the segments γ_T^s and γ_C^s incorporate an additional reparametrization by $\pi/2 - \theta$.

The four curves in Eqs. (35)–(38), together with the two balanced-biaxial points, form the basic skeleton from which we construct a Bezier proto-model of the plane stress yielding surface in the space $(\sigma_{xx}, \sigma_{yy}, \sigma_{xy})$. We do it by interpolating plane sections through the yielding surface with planes $\Pi(\theta)$ defined by:

$$\begin{aligned} \Pi(\theta) &= \{(\sigma_{xx}, \sigma_{yy}, \sigma_{xy}) \in \mathbb{R}^3 \mid (\sigma_{xx} - \sigma_{yy}) \sin(2\theta) = 2\sigma_{xy} \cos(2\theta)\} \\ &= \{\boldsymbol{\sigma} \in \mathbb{R}^3 \mid \boldsymbol{\sigma} \cdot \boldsymbol{\nu}(\theta) = 0\} \end{aligned} \quad (39)$$

where the normal ν is defined by

$$\boldsymbol{\nu}(\theta) = (-\sin(2\theta), \sin(2\theta), \cos(2\theta)), \quad 0 \leq \theta \leq \pi/4 \quad (40)$$

All planes $\Pi(\theta)$ pass through the main diagonal $(\sigma, \sigma, 0)$ and each represents a transformation that renders the stress tensor diagonal along the uniaxial loading frame. Obviously, for any θ the plane $\Pi(\theta)$ intersects each of the above four curves at one unique point. Let θ_T , θ_T^s , θ_C and θ_C^s denote the parameters of the intersection points $P_T = \Pi(\theta) \cap \gamma_T$, $P_T^s = \Pi(\theta) \cap \gamma_T^s$, $P_C = \Pi(\theta) \cap \gamma_C$ and $P_C^s = \Pi(\theta) \cap \gamma_C^s$, respectively. Then one can easily verify that for any $\theta \in [0, \pi/4]$:

$$\theta_T = \theta, \quad \theta_T^s = \frac{\pi}{2} - \theta, \quad \theta_C = \theta, \quad \theta_C^s = \frac{\pi}{2} - \theta \quad (41)$$

Let $B_T = (\bar{\sigma}_{TB}, \bar{\sigma}_{TB}, 0)$ and $B_C = (\bar{\sigma}_{CB}, \bar{\sigma}_{CB}, 0)$ denote the points on the yielding surface corresponding to balanced-biaxial loading in tension and compression, respectively. Then a plane section through the yielding surface defined by the intersection with $\Pi(\theta)$ will be estimated by the following six Bezier segments ordered counterclockwise, where, initially, $\lambda_i = \lambda_i(\theta)$, see Fig. 2:

$$S_1 = \{B_T, \mu_{TB}(\theta), P_T^s(\theta_T^s), \mu_T^s(\theta_T^s), \lambda_1, \lambda_2\}, \quad (42)$$

$$S_2 = \{P_T^s(\theta_T^s), \mu_T^s(\theta_T^s), P_C(\theta_C), \mu_C(\theta_C), \lambda_2, \lambda_3\}, \quad (43)$$

$$S_3 = \{P_C(\theta_C), \mu_C(\theta_C), B_C, \mu_{CB}(\theta), \lambda_3, \lambda_4\}, \quad (44)$$

$$S_4 = \{B_C, \mu_{CB}(\theta), P_C^s(\theta_C^s), \mu_C^s(\theta_C^s), \lambda_4, \lambda_5\}, \quad (45)$$

$$S_5 = \{P_C^s(\theta_C^s), \mu_C^s(\theta_C^s), P_T(\theta_T), \mu_T(\theta_T), \lambda_5, \lambda_6\}, \quad (46)$$

$$S_6 = \{P_T(\theta_T), \mu_T(\theta_T), B_T, \mu_{TB}(\theta), \lambda_6, \lambda_1\} \quad (47)$$

Each curve segment require specification of the two tangent directions. Denoting with P and $\mu(P)$ a generic point of a curve segment and

its corresponding tangent direction, the latter must be in the $\Pi(\theta)$ plane in which P is, and also in the tangent plane of the yielding surface at P . Denoting with $\mathbf{n}(P)$ the exterior unit normal of the yielding surface at P , and recalling the counterclockwise orientation adopted for each patch of curve segments, it follows that the tangent direction at P is determined by the formula

$$\mu(P) = \frac{\mathbf{v}(\theta) \times \mathbf{n}(P)}{|\mathbf{v}(\theta) \times \mathbf{n}(P)|} \quad (45)$$

and it remains to specify the exterior unit normal of the yielding surface at a point P .

At the tensile and compression balanced-biaxial yielding points the tangent plane at the yielding surface is orthogonal to the biaxial plane $\sigma_{xy} = 0$ and hence the exterior unit normal vectors at B_T and B_C are

$$\mathbf{n}_{TB} = \frac{1}{\sqrt{1+r_{TB}^2}}(1, r_{TB}, 0), \quad \mathbf{n}_{CB} = \frac{1}{\sqrt{1+r_{CB}^2}}(-1, -r_{CB}, 0) \quad (46)$$

with r_{TB} and r_{CB} denoting the balanced biaxial r-values in tension and compression, respectively:

$$\begin{aligned} \frac{\partial f}{\partial \sigma_{yy}}(\sigma_{TB}, \sigma_{TB}, 0) &= r_{TB} \frac{\partial f}{\partial \sigma_{xx}}(\sigma_{TB}, \sigma_{TB}, 0), \\ \frac{\partial f}{\partial \sigma_{yy}}(-\sigma_{CB}, -\sigma_{CB}, 0) &= r_{CB} \frac{\partial f}{\partial \sigma_{xx}}(-\sigma_{CB}, -\sigma_{CB}, 0) \end{aligned} \quad (47)$$

Both balanced-biaxial yielding points are thus essential for the construction of the Bezier5YS proto-model. If a balanced-biaxial yielding stress is not available from experiments, then its value is defined as the average

$$\sigma_B = (1/2)(\sigma_0 + \sigma_{90}) \quad (48)$$

where σ_0 and σ_{90} are the tensile/compression uniaxial yield stresses along RD and TD. If a balanced-biaxial r-value is not provided, then its default value is taken as 1.0.⁶

At a point P on a curve γ , with γ denoting here generically any of the four curves in Eqs. (35)–(38), the exterior normal to the yield surface satisfies the r-value relationship

$$[r(\theta) + \sin^2 \theta] \frac{\partial f}{\partial \sigma_{xx}}(\gamma) + [r(\theta) + \cos^2 \theta] \frac{\partial f}{\partial \sigma_{yy}}(\gamma) \pm 2 \cos \theta \sin \theta \frac{\partial f}{\partial \sigma_{xy}}(\gamma) = 0$$

where the '+' branch corresponds to the γ^s curves along which θ is to be replaced by $\pi/2 - \theta$, see Appendix C for details. The exterior unit normal $\mathbf{n}(P)$ thus satisfies

$$\mathbf{w} \cdot \mathbf{n}(P) = 0 \quad (49)$$

where

$$\mathbf{w}(\theta) = (r(\theta) + \sin^2 \theta, r(\theta) + \cos^2 \theta, \pm \sin \theta \cos \theta)$$

Note that the factor of 2 has been dropped since \mathbf{n} is an object of the vector space $(\sigma_{xx}, \sigma_{yy}, \sigma_{xy})$ (and not of the tensor space of σ where the yield function f is defined). At the same time, the curve γ lies on the yielding surface, that is, $f(\gamma(\theta)) = \bar{\sigma}$, and hence differentiation with respect to θ obtains

$$\frac{\partial f}{\partial \sigma_{xx}}(\gamma) \frac{d\gamma_x}{d\theta} + \frac{\partial f}{\partial \sigma_{yy}}(\gamma) \frac{d\gamma_y}{d\theta} + 2 \frac{\partial f}{\partial \sigma_{xy}}(\gamma) \frac{d\gamma_z}{d\theta} = 0 \iff \dot{\gamma} \cdot \mathbf{n}(P) = 0 \quad (50)$$

⁶ In the provided code, these values can be changed in the material data input file. An often employed alternative to Eq. (48) is $\sigma_B = (1/4)(\sigma_0 + 2\sigma_{45} + \sigma_{90})$. The author is not aware of any theoretical motivation for these averaging formulas. The balanced-biaxial r-value also can be assigned by similar formulas. Note, however, that while for balanced-biaxial yielding stresses the two averaging formulas provide similar results, in the case of r-values, the two estimates may differ significantly, as one can easily observe for the two aluminum alloys in tables Appendix E/6 and 7.

Since the vector \mathbf{w} is always pointing into the first quadrant, from the last two equations it follows that

$$\mathbf{n}(P) = \frac{\mathbf{w} \times \dot{\gamma}}{|\mathbf{w} \times \dot{\gamma}|} \quad (51)$$

The above formula reveals for the first time in an explicit form the relationship between r-values and the exterior unit normal of the yield surface at all points of the curves traced on the yield surface by the uniaxial tests. Notice that it does not depend on the parametrization of γ .

• Shape parameters and convexity of plane sections

The most general parametrization of Bezier5YS requires specification of the six shape parameter functions $\lambda_i = \lambda_i(\theta)$, for $\theta \in [0, \pi/4]$. This is a daunting task not only because of the lack of data (which Bezier5YS is supposed to deliver in the first place), but also because of continuity and convexity constraints. We simplify by assuming constant shape parameter functions: $\lambda_i(\theta) = \Lambda_i = ct$. Then as the $\Pi(\theta)$ -section rotates towards the vertical section $\theta = 45^\circ$, symmetry with respect to the $\sigma_{xy} = 0$ plane and continuity of the surface require that: $\Lambda_3 = \Lambda_1$, $\Lambda_4 = \Lambda_6$. Thus, upon renumbering the Λ_i parameters, the general patch described in Eqs. (42)–(44) is employed with the following pairs of shape parameters.

$$S_1 : (\Lambda_1, \Lambda_2), S_2 : (\Lambda_2, \Lambda_1), S_3 : (\Lambda_1, \Lambda_3),$$

$$S_4 : (\Lambda_3, \Lambda_4), S_5 : (\Lambda_4, \Lambda_3), S_6 : (\Lambda_3, \Lambda_1)$$

In particular, on the $\Pi(\theta = 0^\circ)$ section, the biaxial curve, Λ_1 controls the shape of the curve in the vicinity of the tension RD and TD points, Λ_2 controls the shape in the vicinity of the tension balanced-biaxial point, and Λ_3 and Λ_4 control the shape in the vicinity of compression RD, TD and balanced-biaxial points, respectively. In case of tension-compression symmetry, the number of shape parameters is further reduced by the relationships $\Lambda_1 = \Lambda_3$ and $\Lambda_2 = \Lambda_4$, and hence the symmetric Bezier5YS has two shape parameters.

The upper bound of each shape parameter is determined by requiring that every Bezier patch of curve segments be convex. This will ensure the convexity of $\Pi(\theta)$ -plane sections but not necessarily the overall convexity of the Bezier5YS surface. This is not a concern here since the identification procedure for SHYqp will enforce overall convexity based on constraints and hence the basic consistency of the data generated by Bezier5YS with convex plane sections is sufficient.

Then let us consider a segment γ specified as in Eq. (31). For our purposes, yield surface modeling, the two end unit directions must point in the same direction as $B_5 - B_0$:

$$\mu_S \cdot (B_E - B_S) \geq 0, \quad \mu_E \cdot (B_E - B_S) \geq 0 \quad (52)$$

In particular, it follows that

$$\mu_S \cdot \mu_E \in [0, 1] \quad (53)$$

Next, it is known that a Bezier curve lies within the convex closure of its control polygon. In our case, the necessary and sufficient condition for a segment to be convex is that the control polygon itself be convex. Then letting $d_S = \{B_0 + t\mu_S \mid t \geq 0\}$ and $d_E = \{B_5 - \tau\mu_E \mid \tau \geq 0\}$ denote the half-lines determined by the two end points and unit directions, respectively, their intersection $d_S \cap d_E$ is determined by:

$$B_0 + t\mu_S = B_5 - \tau\mu_E \quad (54)$$

Taking the dot product with μ_S and μ_E obtains the linear system:

$$\begin{cases} t + (\mu_S \cdot \mu_E)\tau &= (B_E - B_S) \cdot \mu_S \\ (\mu_S \cdot \mu_E)t + \tau &= (B_E - B_S) \cdot \mu_E \end{cases}$$

If $\mu_S \cdot \mu_E = 1$, the two equations become identical to $t + \tau = |B_E - B_S|$ and it follows that the maximum value λ_{max} is determined by $2\lambda_{max} +$

$2\lambda_{max} = |B_E - B_S|$, i.e., $0 < \lambda < |B_E - B_S|/4$. If $\mu_S \cdot \mu_E < 1$, the above two equations can be solved for t and τ :

$$t = \frac{1}{1 - \mu_S \cdot \mu_E} (B_E - B_S) \cdot [\mu_S - (\mu_S \cdot \mu_E)\mu_E] \quad (55)$$

$$\tau = \frac{1}{1 - \mu_S \cdot \mu_E} (B_E - B_S) \cdot [\mu_E - (\mu_S \cdot \mu_E)\mu_S] \quad (56)$$

t is the maximum admissible value for $2\lambda_S$ when constructing point B_2 defined by Eq. (29); similarly, τ is the maximum admissible value for $2\lambda_E$ when constructing point B_3 defined by Eq. (30). Thus a curve segment γ is convex if and only if its shape parameters are confined to the intervals

$$0 \leq \lambda_S \leq \frac{\tau}{2}, \quad 0 \leq \lambda_E \leq \frac{\tau}{2} \quad (57)$$

Then the intervals $[0, \Lambda_i^{max}]$ of variation of the overall shape parameters of the Bezier5YS interpolated surface are the intersection of all the above corresponding intervals, on every $\Pi(\theta)$ -plane section.

If, for some $\Pi(\theta)$ section the value of λ_S , or λ_E , of a segment is negative, then the corresponding $\Lambda^{max} < 0$, meaning that the input experimental data is not compatible with a convex shape. In this case, the provided Python implementation triggers a ‘fatal’ warning and aborts calculations.

Finally, the desired shape parameters Λ_i of a Bezier5YS proto-model are specified as fractions of their corresponding maximal admissible values Λ_i^{max} :

$$\Lambda_i = s_i \Lambda_i^{max} \quad (58)$$

where $s_i \in [0, 1]$ are scaling factors. In the extreme case of all $\Lambda_i = 0$, the Bezier5YS proto-model is simply the boundary of the convex hull of the uniaxial curves and balanced-biaxial points — the limiting case of a Tresca-like polyhedron. When all $s_i = 1$, the Bezier5YS surface has the highest possible overall curvature.

• Some illustrations of Bezier5YS proto-models

When only the basic experimental data set is available, with no additional information on the overall shape of the yield surface, the most straightforward approach is to use the simplest proto-model, the one obtained by setting all shape parameters equal to a common value Λ ; Then necessarily, to retain the convexity of all plane sections: $\Lambda = \min\{\Lambda_i\}$. This condition is strong: The resulting surface has the overall curvature of its tightest segment. It is in this simplest case that we show some examples of Bezier5YS proto-models, although quite abstract, but nevertheless representative for the main crystal lattices.

Fig. 3 illustrates the influence of Λ on the overall shape of the proto-model in the case of isotropic symmetric mechanical properties (all $\bar{\sigma}_\theta = 1$ and all $r_\theta = 1$): on the left, the proto-model is almost identical with the von Mises quadratic,⁷ while on the right the proto-model resembles a high-order (Hershey, 1954; Hill and Hutchinson, 1992; Hosford, 1972) like surface. The magnitude of the maximal admissible value in this case is instructive, since it may be taken as a reference value (representative for steels): $\Lambda^{max} \approx 0.167$.

Fig. 4 shows the proto-models of the aluminum alloys AA5042-H2 (data in Appendix E/Table 6) and AA2090-T3 (data in Appendix E/Table 7). The ranges of the shape parameter of the two alloys are significantly smaller: $\Lambda^{max} \approx 0.072$ and $\Lambda^{max} \approx 0.096$, respectively. This is consistent with the tighter yield surface shapes featured by aluminum alloys.

Finally, Fig. 5 shows the proto-models of the Ti-CP Grade 4 alloy (data from Appendix E/Table 5) and of the magnesium alloy AZ31B (data from Appendix E/Table 3). The titanium alloy is ‘steel-like’ with

respect to its shape parameter: $\Lambda_{max} \approx 0.147$. On the other hand, AZ31B has a very small upper bound for shape variation, $\Lambda_{max} \approx 0.047$, and hence the polyhedral shape of its proto-model.

5. Convexity of SHYqp

In classical (associate) plasticity, the yield surface also determines the increment of plastic strain at a yielding stress state via the normality rule: the plastic strain rate is assumed to be in the direction of the external normal of the yield surface at the current stress. Then a local one-to-one relationship between a yielding stress and an increment of plastic deformation exists if the yield surface is (strictly) convex. Here we deduce some general results, regarding the convexity of the function defined by Eq. (17). The only assumptions are that P and Q are homogeneous polynomials in the 5 variables s_1, s_2, s_3, s_4, s_5 .

Formula (101) of Appendix B shows that f , as a function of the stress tensor σ is convex if and only if \hat{f} is convex, as a function of the stress deviator s . The component form of the Hessian of \hat{f} , as expressed by formula (123) of Appendix B, can be conveniently rewritten in tensor form as:

$$\begin{aligned} \mathbf{H}(s) &= \frac{\sqrt{3}}{|s|\sqrt{2}} \left\{ d_1(\mathbf{u})\mathbf{I} + d_2(\mathbf{u})\mathbf{u} \otimes \mathbf{u} - (n_P - 1)[\mathbf{u} \otimes \mathbf{D}_P(\mathbf{u}) + \mathbf{D}_P(\mathbf{u}) \otimes \mathbf{u}] \right. \\ &\quad \left. - (n_Q - 1)[\mathbf{u} \otimes \mathbf{D}_Q(\mathbf{u}) + \mathbf{D}_Q(\mathbf{u}) \otimes \mathbf{u}] + \mathbf{H}_P(\mathbf{u}) + \mathbf{H}_Q(\mathbf{u}) \right\} \end{aligned} \quad (59)$$

where \mathbf{I} is the identity tensor of $\mathbb{S} \approx \mathbb{R}^5$, and where P and Q are generic notations for P_{2m-1} and P_{2m} , respectively, \mathbf{D}_P and \mathbf{D}_Q for their gradients, and \mathbf{H}_P and \mathbf{H}_Q for their Hessian matrices/tensors; Also, we denote by

$$d_1(\mathbf{u}) = 1 - (n_P - 1)P(\mathbf{u}) - (n_Q - 1)Q(\mathbf{u}) \quad (60)$$

$$d_2(\mathbf{u}) = (n_P^2 - 1)P(\mathbf{u}) + (n_Q^2 - 1)Q(\mathbf{u}) - 1 \quad (61)$$

with $n_P = 2m - 1$ and $n_Q = 2m$.

It is seen from Eq. (59) that \hat{f} is convex if and only if the restriction of its Hessian to the unit sphere of \mathbb{S} is semi-positive definite, that is:

$$[\mathbf{H}(\mathbf{u}) : \mathbf{v}] \cdot \mathbf{v} \geq 0, \quad \forall \mathbf{u} \in U, \quad \forall \mathbf{v} \in \mathbb{S} \quad (62)$$

where “ $:$ ” signifies the operation of applying a tensor to a vector, and “ \cdot ” represents the dot product. Since \mathbf{H} depends linearly on the vectors of parameters $\mathbf{c}_P = \{c_P^i\}$ and $\mathbf{c}_Q = \{c_Q^j\}$, the above leads to the following representation of K - the set of parameters for which the analytical expression in Eq. (17) is convex:

$$K = \bigcap_{\mathbf{u} \in U} \bigcap_{\mathbf{v} \in \mathbb{S}} \{(\mathbf{c}_P, \mathbf{c}_Q) | \mathbf{c}_P \cdot \mathbf{w}_P(\mathbf{u}, \mathbf{v}) + \mathbf{c}_Q \cdot \mathbf{w}_Q(\mathbf{u}, \mathbf{v}) + a(\mathbf{u}, \mathbf{v}) \geq 0\}$$

where \mathbf{w}_P , \mathbf{w}_Q and a denote entities that depend only on \mathbf{u} and \mathbf{v} . Thus K is an intersection of half-spaces and hence we have obtained the following important result: **the set of parameters for which f is convex is itself a convex set**.

Next, let us decompose \mathbf{v} as $\mathbf{v} = \mathbf{v}^\perp + \lambda\mathbf{u}$, with $\mathbf{v}^\perp \cdot \mathbf{u} = 0$ (Note that $\mathbf{v}^\perp = \mathbf{v}^\perp(\mathbf{u})$, since \mathbf{v}^\perp is the projection of \mathbf{v} on the tangent hyper-plane of the unit sphere at \mathbf{u}). Then:

$$(\mathbf{H} : \mathbf{v}) \cdot \mathbf{v} = (\mathbf{H} : \mathbf{v}^\perp) \cdot \mathbf{v}^\perp + 2\lambda(\mathbf{H} : \mathbf{u}) \cdot \mathbf{v}^\perp + \lambda^2(\mathbf{H} : \mathbf{u}) \cdot \mathbf{u} \quad (63)$$

We recall now that for a homogeneous polynomial P of degree n_P there hold the following relations⁸:

$$\mathbf{D}_P(\mathbf{u}) \cdot \mathbf{u} = n_P P(\mathbf{u}), \quad \mathbf{H}_P(\mathbf{u}) : \mathbf{u} = (n_P - 1)\mathbf{D}_P(\mathbf{u})$$

⁷ We note that an exact match of the quadratic is not possible with Bezier5YS. A reformulation based on NURBS, instead of Bezier curves, does include the quadratic as a particular case. However, in the context of a data generating scheme the Bezier representation is sufficient. In addition, SHYqp itself includes von Mises as a particular case.

⁸ The second one may be less known. It is obtained by differentiating with respect to s_j the relationship $\partial P / \partial s_i(\lambda s) s_i = n \lambda^{n_P-1} P(s)$, holding for all $\lambda > 0$ and all s .

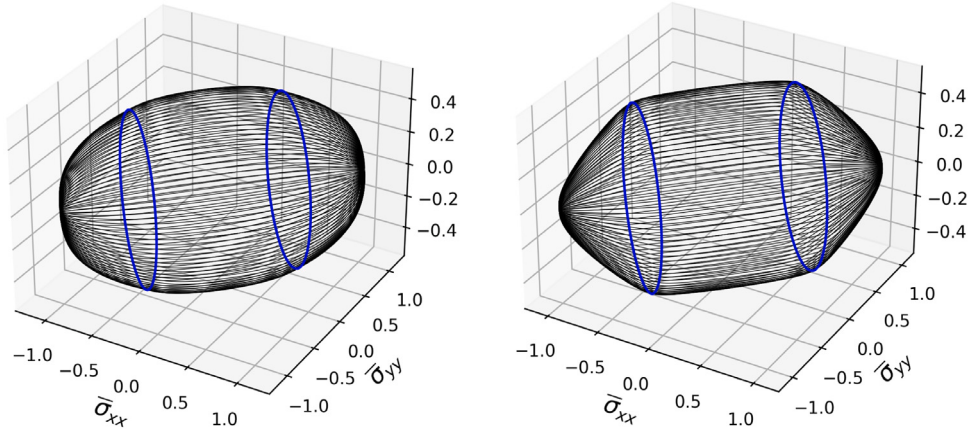


Fig. 3. Plot of the Bezier5YS proto-model for isotropic symmetry. The two blue curves on each surface represent the uniaxial tensile and compression curves. Left: $s = 100\%$; Right: $s = 50\%$. Note: in all 3D surface plots featured in this work, $\bar{\sigma}_{xy}$ is on the third (vertical) axis. (For interpretation of the references to color in this figure legend, the reader is referred to the web version of this article.)

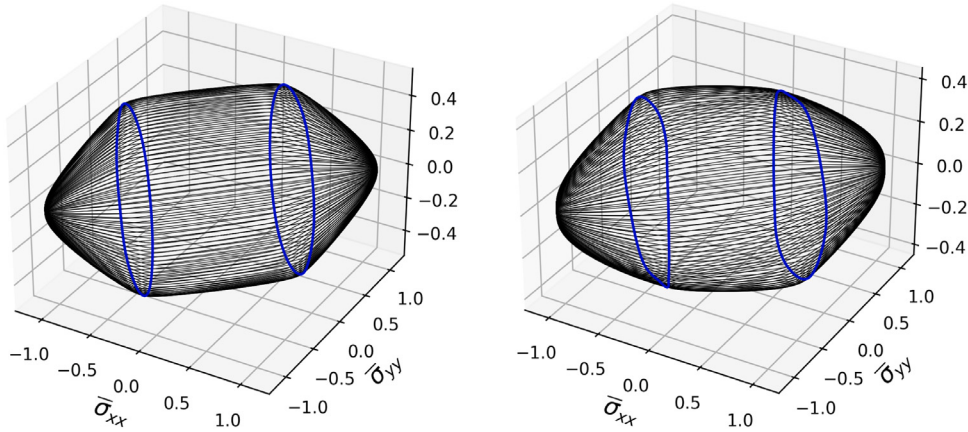


Fig. 4. Bezier5YS proto-models of two aluminum alloys: AA5042-H2 (Left) and AA2090-T3 (Right). For both: $s = 100\%$.

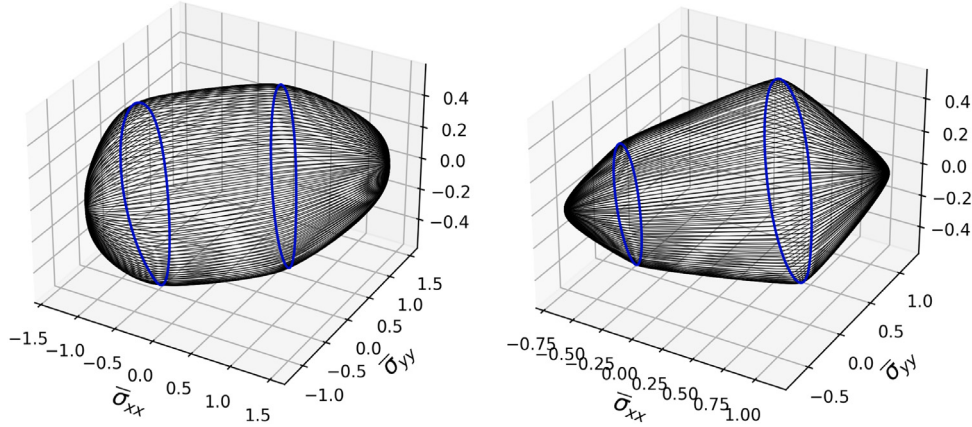


Fig. 5. Bezier5YS proto-models of titanium Ti-CP (Left) and AZ31B (Right). Both: $s = 100\%$.

These and Eq. (59) obtain:

$$(\mathbf{H} : \mathbf{u}) \cdot \mathbf{u} = \sqrt{\frac{3}{2}} [d_1(\mathbf{u}) + d_2(\mathbf{u}) - (n_P - 1)n_P P(\mathbf{u}) - (n_Q - 1)n_Q Q(\mathbf{u})] = 0$$

$$\begin{aligned} (\mathbf{H} : \mathbf{u}) \cdot \mathbf{v}^\perp &= \sqrt{\frac{3}{2}} [\mathbf{H}_P(\mathbf{u}) : \mathbf{u} - (n_P - 1)\mathbf{D}_P(\mathbf{u}) \\ &\quad + \mathbf{H}_Q(\mathbf{u}) : \mathbf{u} - (n_Q - 1)\mathbf{D}_Q(\mathbf{u})] \cdot \mathbf{v}^\perp = 0 \end{aligned}$$

Thus Eq. (63) reduces to

$$(\mathbf{H} : \mathbf{v}) \cdot \mathbf{v} = (\mathbf{H} : \mathbf{v}^\perp) \cdot \mathbf{v}^\perp \tag{64}$$

Then, $\mathbf{H}(\mathbf{u})$ is positive semi-definite if Eq. (62) is satisfied by all vectors \mathbf{v}^\perp that are tangent to the unit sphere U at \mathbf{u} . Substituting this back into Eq. (59), results in the following: The function defined by Eq. (17) is convex if and only if the restricted hessian $\widehat{\mathbf{H}}$ defined by

$$\widehat{\mathbf{H}}(\mathbf{u}) = d_1(\mathbf{u})\mathbf{I} + \mathbf{H}_P(\mathbf{u}) + \mathbf{H}_Q(\mathbf{u}) \tag{65}$$

is semi-positive definite on the tangent hyper-plane of the unit sphere at \mathbf{u} . The convexity of SHYqp can then be easily managed numerically by enforcing the above formula at a sufficiently dense cloud of points on the unit sphere of \mathbb{S} to obtain a discrete set of linear constraints on (c_P, c_Q) . The specific details are presented in [Appendix D](#).

6. SHYqp parameter identification

In the minimalist case, when only three directional tests may be available (for both tension and compression), the corresponding equations for yielding and r-values can uniquely determine the parameters of SHYqp only if the degree of its even component is at most $n_Q = 4$: In this case there are 15 parameters and 12 directional equations for yielding stresses and r-values, with additional data points sampled as needed from balanced-biaxial tests. As discussed in [Soare \(2022\)](#), this *pointwise* approach to parameter identification – the design paradigm of conventional yield functions – where the yield function parameters are calibrated by a specific combination of data points, limits considerably the control over the overall quality (precision) of the yield surface model and is subjective (by emphasizing specific data points). The natural approach to parameter identification is to employ every available data point to obtain an over-determined system of equations which can then be solved by optimizing its associate cost function.

The parameters of the SHYqp model are identified by minimizing the weighted distance between its prediction and the proto-model generated by the Bezier5YS model. Since the relationship between the input data and the parameters of SHYqp is linear, this amounts to solving a (constrained) quadratic optimization problem. In particular, the solution is always unique. Furthermore, the convexity of the corresponding yield surface is ensured by enforcing a set of constraints as discussed in the previous section and [Appendix D](#). It is worth emphasizing that, by contrast with polynomial yield functions, where the optimization problem in its most general form is quadratic with quadratic constrains, here the constraints are all linear. The latter problem is a classic topic in optimization theory, and many algorithms are available. The code accompanying this article employs (as options) the Python optimization libraries quadprog, [Goldfarb and Idnani \(1983\)](#), and cvxopt, [Boyd and Vandenberghe \(2004\)](#). The details of the formulation of the optimization problem as a quadratic problem are presented next.

The context here is plane stress, where $\sigma_{zz} = \sigma_{xz} = \sigma_{yz} = 0$ and the objective is the identification of the parameters c_{P1} and c_{Q1} of the expression in Eq. [\(17\)](#). Recalling that $\bar{\sigma}_{T\theta}$ and $\bar{\sigma}_{C\theta}$ denote the yield stresses in uniaxial traction and compression tests, the corresponding stress states are given by formulas in Eqs. [\(35\)](#) and [\(37\)](#). Then with Eqs. [\(7\)](#)–[\(8\)](#), the corresponding deviatoric components of s_T are

$$s_{T1} = (\bar{\sigma}_{T\theta}/\sqrt{6})(2\cos^2\theta - \sin^2\theta), \quad s_{T2} = (\bar{\sigma}_{T\theta}/\sqrt{2})\sin^2\theta,$$

$$s_{T3} = \bar{\sigma}_{T\theta}\sqrt{2}\sin\theta\cos\theta$$

for points along γ_T , where we also have $|s_T| = \bar{\sigma}_T(\theta)\sqrt{2/3}$, while those of s_C are

$$s_{C1} = (\bar{\sigma}_{C\theta}/\sqrt{6})(-2\cos^2\theta + \sin^2\theta), \quad s_{C2} = -(\bar{\sigma}_{C\theta}/\sqrt{2})\sin^2\theta,$$

$$s_{C3} = -\bar{\sigma}_{C\theta}\sqrt{2}\sin\theta\cos\theta$$

for points along γ_C , where $|s_C| = \bar{\sigma}_C(\theta)\sqrt{2/3}$. Then the corresponding unit stress vectors $\mathbf{u} = s/|s|$ along the two curves have the components

$$u_{T1} = \cos^2\theta - (1/2)\sin^2\theta, \quad u_{T2} = (\sqrt{3}/2)\sin^2\theta, \quad u_{T3} = \sqrt{3}\sin\theta\cos\theta \quad (66)$$

and

$$u_{C1} = -\cos^2\theta + (1/2)\sin^2\theta, \quad u_{C2} = -(\sqrt{3}/2)\sin^2\theta, \quad u_{C3} = -\sqrt{3}\sin\theta\cos\theta \quad (67)$$

Requiring that the yield surface passes through the tensile and compression test points obtains the equations

$$P(\mathbf{u}_T(\theta_{Tk})) + Q(\mathbf{u}_T(\theta_{Tk})) = \frac{1}{\bar{\sigma}_{T\theta_k}} - 1, \quad k = 0, \dots, N_T \quad (68)$$

$$P(\mathbf{u}_C(\theta_{Ck})) + Q(\mathbf{u}_C(\theta_{Ck})) = \frac{1}{\bar{\sigma}_{C\theta_k}} - 1, \quad k = 0, \dots, N_C \quad (69)$$

Considering next the r-values of the material, we shall need the gradient of the yield function. With calculations detailed in [Appendix A](#), the components relevant to the identification procedure are given by the formulas

$$\frac{\partial f}{\partial \sigma_{xx}} = \sqrt{\frac{2}{3}} \frac{\partial \hat{f}}{\partial s_1}, \quad \frac{\partial f}{\partial \sigma_{yy}} = \frac{1}{\sqrt{2}} \frac{\partial \hat{f}}{\partial s_2} - \frac{1}{\sqrt{6}} \frac{\partial \hat{f}}{\partial s_1}, \quad \frac{\partial f}{\partial \sigma_{xy}} = \frac{1}{\sqrt{2}} \frac{\partial \hat{f}}{\partial s_3} \quad (70)$$

where

$$\frac{\partial \hat{f}}{\partial s_k}(s) = \sqrt{\frac{3}{2}} \left\{ u_k [1 - (n_P - 1)P(\mathbf{u}) - (n_Q - 1)Q(\mathbf{u})] + \frac{\partial P}{\partial s_k}(\mathbf{u}) + \frac{\partial Q}{\partial s_k}(\mathbf{u}) \right\} \quad (71)$$

The r-value equation reads

$$(r_\theta + \sin^2\theta) \frac{\partial f}{\partial \sigma_{xx}}(\gamma) + (r_\theta + \cos^2\theta) \frac{\partial f}{\partial \sigma_{yy}}(\gamma) - 2\sin\theta\cos\theta \frac{\partial f}{\partial \sigma_{xy}}(\gamma) = 0 \quad (72)$$

where $\gamma(\theta)$ is a point on either of the curves in Eqs. [\(35\)](#) and [\(37\)](#). To simplify notation, we shall denote $\alpha = r_\theta + \sin^2\theta$, $\beta = r_\theta + \cos^2\theta$ and $\omega = \cos\theta\sin\theta$. Requiring that the r-value equation hold at all directional data points obtains, after some straightforward manipulations of Eqs. [\(70\)](#)–[\(72\)](#),

$$\begin{aligned} \zeta(n_P - 1)P + \left(\alpha - \frac{\beta}{2}\right) \frac{\partial P}{\partial s_1} + \frac{\beta\sqrt{3}}{2} \frac{\partial P}{\partial s_2} - \omega\sqrt{3} \frac{\partial P}{\partial s_3} + \zeta(n_Q - 1)Q \\ + \left(\alpha - \frac{\beta}{2}\right) \frac{\partial Q}{\partial s_1} + \frac{\beta\sqrt{3}}{2} \frac{\partial Q}{\partial s_2} - \omega\sqrt{3} \frac{\partial Q}{\partial s_3} = \zeta \end{aligned} \quad (73)$$

where we denoted by $\zeta = -(\alpha - \beta/2)u_1 - (\beta\sqrt{3}/2)u_2 + \omega\sqrt{3}u_3$. In the general, asymmetric case, the above equation is enforced for both sets of sampling locations in Eqs. [\(66\)](#) and [\(67\)](#).

Since the yielding data points are normalized by $\bar{\sigma}_{T0}$, the optimized parameters should reproduce this normalization. In fact, this can be achieved analytically because Eqs. [\(68\)](#) and [\(69\)](#) can be solved explicitly for c_{P1} and c_{Q1} when $\theta = 0$ to obtain

$$c_{Q1} = \frac{1}{2} \left(\frac{1}{\bar{\sigma}_{C0}} - 1 \right), \quad c_{P1} = -c_{Q1} \quad (74)$$

We go one step further and also solve the two equations resulting from Eq. [\(73\)](#) in the case $\theta = 0$ for tension and compression to obtain:

$$\begin{aligned} c_{Q2} &= \frac{1}{2\sqrt{3}} \left[\frac{1 - r_{T0}}{1 + r_{T0}} + \frac{1 - r_{C0}}{(1 + r_{C0})\bar{\sigma}_{C0}} \right], \\ c_{P2} &= \frac{1}{2\sqrt{3}} \left[\frac{1 - r_{T0}}{1 + r_{T0}} - \frac{1 - r_{C0}}{(1 + r_{C0})\bar{\sigma}_{C0}} \right] \end{aligned} \quad (75)$$

Remarkably, the coefficients c_{P1} , c_{Q1} , c_{P2} and c_{Q2} have a ‘universal’ character: they are the same for P and Q of any degree. These coefficients enforce exactly the yielding points and the r-values along RD and are not subject to optimization.

The above work-flow repeats with minor adaptations for balanced-biaxial stress states $\sigma = \bar{\sigma}(1, 1, 0)$, where $\bar{\sigma}$ is either $\bar{\sigma}_{TB}$ or $-\bar{\sigma}_{CB}$, to obtain:

$$s_1 = \bar{\sigma}/\sqrt{6}, \quad s_2 = \bar{\sigma}/\sqrt{2}, \quad s_3 = 0, \quad |s| = |\bar{\sigma}|\sqrt{2/3}$$

$$\Rightarrow u_1 = \pm 1/2, \quad u_2 = \pm\sqrt{3}/2, \quad u_3 = 0$$

Then requiring that the yield surface passes through the two balanced-biaxial yielding stresses obtains:

$$P(1/2, \sqrt{3}/2, 0) + Q(1/2, \sqrt{3}/2, 0) = \frac{1}{\bar{\sigma}_{TB}} - 1 \quad (76)$$

$$P(-1/2, -\sqrt{3}/2, 0) + Q(-1/2, -\sqrt{3}/2, 0) = \frac{1}{\bar{\sigma}_{CB}} - 1 \quad (77)$$

On rare occasions, the r-values for the balanced-biaxial tests are also measured to provide an equation of the form

$$-r_B \frac{\partial f}{\partial \sigma_{xx}}(\bar{\sigma}, \bar{\sigma}, 0) + \frac{\partial f}{\partial \sigma_{yy}}(\bar{\sigma}, \bar{\sigma}, 0) = 0$$

with r_B being either r_{TB} or r_{CB} and $\bar{\sigma}$ either $\bar{\sigma}_{TB}$ or $-\bar{\sigma}_{CB}$, respectively. For SHYqp the above equation becomes

$$\begin{aligned} \zeta(n_P - 1)P - \left(r_B + \frac{1}{2}\right) \frac{\partial P}{\partial s_1} + \frac{\sqrt{3}}{2} \frac{\partial P}{\partial s_2} \\ + \zeta(n_Q - 1)Q - \left(r_B + \frac{1}{2}\right) \frac{\partial Q}{\partial s_1} + \frac{\sqrt{3}}{2} \frac{\partial Q}{\partial s_2} = \zeta \end{aligned} \quad (78)$$

where this time $\zeta = (r_{TB} - 1)/2$ for tension, and $\zeta = (1 - r_{CB})$ for compression.

Finally, denoting by

$$\sigma^Z = (\sigma_{xx}^Z, \sigma_{yy}^Z, \sigma_{xy}^Z) \quad (79)$$

an arbitrary point on the proto-model yield surface, its corresponding image in the deviatoric \mathbb{S} space is $s^Z = s_1^Z \mathbf{g}_1 + s_2^Z \mathbf{g}_2 + s_3^Z \mathbf{g}_3$ where

$$s_1^Z = (2\sigma_{xx}^Z - \sigma_{yy}^Z)/\sqrt{6}, \quad s_2^Z = \sigma_{yy}^Z/\sqrt{2}, \quad s_3^Z = \sigma_{xy}^Z/\sqrt{2} \quad (80)$$

Then requiring the SHYqp yield surface to pass through the point σ^Z obtains

$$\sqrt{\frac{3}{2}}|s^Z| [1 + P(u^Z) + Q(u^Z)] = \sigma_{T0} \iff P(u^Z) + Q(u^Z) = \frac{1}{|s^Z|\sqrt{3/2}} - 1 \quad (81)$$

where $u^Z = s^Z/|s^Z|$. In the second equation we used the fact that the proto-model is already normalized (and hence $\sigma_{T0} = 1$).

Eqs. (68), (69), (73), (76), (77) and (78) admit a general representation in the form

$$\sum_k A_{jk}^{(Y)} c_k = b_j^{(Y)}, \quad j = 1, \dots, N^{(Y)} \quad (82)$$

where c_k are the coefficients c_p^i and c_Q^i ordered in a common list for $i \geq 3$ (because c_p^1, c_p^2, c_Q^1 and c_Q^2 are calculated explicitly by the formulas in Eqs. (74) and (75)). The superscript notation (Y) is used here to indicate that these equations enforce the actual experimental data. Here $N^{(Y)} = N_{data} - 4$, where N_{data} is the total number of data points and hence, as discussed previously, the above linear system is in general under-determined.

The additional Eqs. (81) extracted from the proto-model can be rewritten also in the form

$$\sum_k A_{jk}^{(Z)} c_k = b_j^{(Z)}, \quad j = 1, \dots, N^{(Z)} \quad (83)$$

The number $N^{(Z)}$ of data points σ^Z can be adjusted to support any number of parameters for SHYqp. As a rule, $N^{(Z)}$ should be at least as large as the total number of parameters of SHYqp. This ensures that the combined system (82) and (83) is always over-determined. However, since the number of Z-equations is usually much larger than the number of Y-equations, the accuracy of the SHYqp fitting of the latter group of equations can be affected. Therefore we shall have to discern between actual data points and proto-model points by assigning different weights to their corresponding equations. These weights are scaled uniformly to form a binary partition of the data: an overall weight $w^{(Y)} > 0$ is assigned to all actual data points (which is further distributed, internally, with ratios of $0.8w^{(Y)}$ to stresses and of $0.2w^{(Y)}$ to r-values, uniformly) and an overall weight $w^{(Z)} > 0$ to all proto-model data points such that $w^{(Y)} + w^{(Z)} = 1$. Then Y-equations, corresponding

to actual data points, and Z-equations, corresponding to proto-model points, are weighted by

$$w_j^{(Y)} = \frac{w^{(Y)}}{N^{(Y)}}, \quad w_j^{(Z)} = \frac{w^{(Z)}}{N^{(Z)}} \quad (84)$$

respectively.

Finally, the system (82)–(83) is rewritten in the form $A : c = b$, where the matrix A is constructed by stacking row-wise the matrices $A^{(Y)}$ and $A^{(Z)}$. The corresponding weights are assembled into the diagonal matrix

$$W = \text{Diag}(w_1^{(Y)}, \dots, w_{N^{(Y)}}^{(Y)}, w_1^{(Z)}, \dots, w_{N^{(Z)}}^{(Z)})$$

Then the cost function associated with the system (82)–(83) weighted by (84) is

$$J(c_k) = \frac{1}{2} \sum_j W_{jj} |(A : c - b)_j|^2 = \frac{1}{2} [WA : x - W : b] \cdot (A : c - b)$$

Straightforward manipulations transform the above into the classical quadratic form employed by most optimization algorithms

$$J(c_k) = \frac{1}{2} (A^T WA : c) \cdot c - (A^T W : b) \cdot c \quad (85)$$

where the constant term $(1/2)(W : b) \cdot b$ has been dropped since it does not affect the optimization process. In addition, the vector of coefficients $c = (c_k)_k$ is subject to convexity constraints of the form

$$F : c \leq f \quad (86)$$

where the matrix F and the column vector f are constructed row-wise by using Eq. (136) of Appendix D.

We close this section with a remark regarding the experimental data used for parameter identification. We restricted this data set to the traditional ‘directional’ (plus balanced-biaxial) description simply because this is the one most often employed in practice or reported in the specialized literature. The identification procedure can be easily extended to incorporate virtually any type of experiment by extending the set of Y-relations with appropriate equations. This option has been implemented in SHYqp by allowing for the specification of additional yielding data points and is illustrated in Section 8. An alternative is to directly extend the Bezier5YS proto-model. This approach, however, requires a more careful handling, since data needs to be distributed in a specific pattern and also be compatible with a convex shape.

7. Applications to metallic alloys

Bezier5YS and SHYqp are amenable to a fully automated -user friendly - operational procedure: The basic input required from the user is the experimental data and the degree n_Q . The additional meta-parameters of Bezier5YS and SHYqp have the following default values (which can be changed via an input file):

- Bezier5YS averaging parameter in Eq. (32) for tangent directions: $\mu = 1/2$
- Bezier5YS scaling parameter in Eq. (34) for directional properties: $s = 60\%$
- Bezier5YS with one shape parameter: scaling for Λ_{max} obtained via Eq. (57) is $s = 100\%$
- SHYqp weight parameter in Eq. (84): $w^{(Y)} = 0.9$ (the influence of the proto-model is quite strong, so for lower degrees, e.g., $n_Q \leq 10$, one may also use $w^{(Y)} = 0.95$ to improve the fit of the actual data)
- SHYqp number of constraint points along the biaxial curve in the $\sigma_{xy} = 0$ plane (see Appendix D): 200
- SHYqp lower bound on constraints hessian values (see Appendix D): $\epsilon = 0.01$ (For numerical stability; Side-effect: smoother vertices than implied by actual data)

Table 1

Performance and additional info on the SHYqp models shown in this section (Figs. 6–19): the SHYqp degree n_Q used, the minimum value \det of all leading principal minors, the minimum value K_G of the Gaussian curvature, performance measures Δ_Σ and Δ_R , and balanced-biaxial data vs predictions (in the format *experiment | predicted*; We recall that missing experimental values in this case were inferred (for stresses) or assumed (for strain ratios)).

Material	Data	n_Q	\det	K_G	Δ_Σ	Δ_R	$\bar{\sigma}_{TB}$	r_{TB}	$\bar{\sigma}_{CB}$	r_{CB}
AZ31B	Table 3	4	-1.4e-14	0.0679	0.0826	0.6146	1.085 1.016	1.000 0.485	0.652 0.612	1.000 0.671
AZ31B	Table 3	14	-4.4e-13	0.0009	0.0410	0.3419	1.085 1.047	1.000 0.807	0.652 0.638	1.000 0.718
AZ31B	Table 4	14	-1.8e-13	0.0010	0.0460	0.1074	0.934 0.913	1.000 0.894	0.796 0.755	1.000 0.987
Ti-CP	Table 5	10	-3.8e-14	0.0013	0.0037	0.0174	1.406 1.403	1.000 0.983	1.065 1.067	1.000 1.005
AA5042H2	Table 6	16	-4.6e-14	0.0008	0.0018	0.0026	1.072 1.070	0.991 0.990	—	—
AA2090T3	Table 7	16	-1.0e-13	0.0008	0.0043	0.0079	1.035 1.038	0.670 0.675	—	—
DP980	Table 8	8	-2.7e-15	0.0917	0.0079	0.0417	1.021 1.016	1.000 0.971	—	—

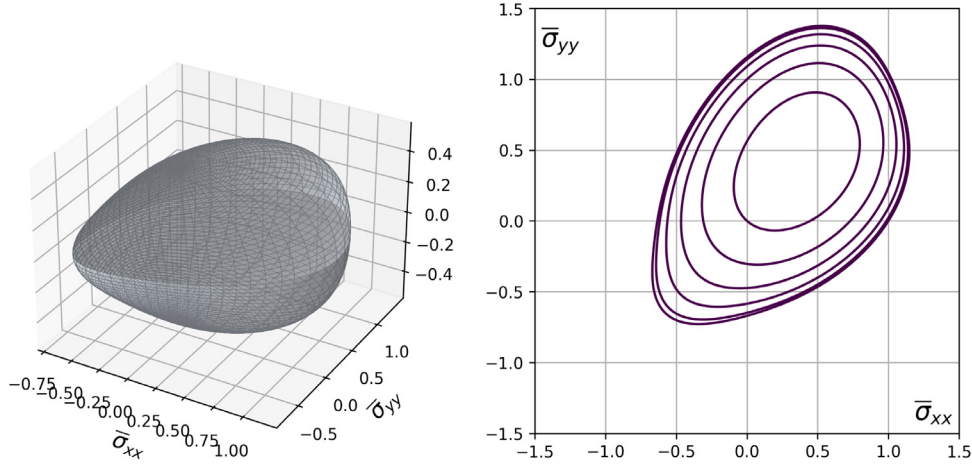


Fig. 6. AZ31B/Lou et al. (2007) ($n_Q = 4$): Predicted yield surface and several horizontal sections. This is the famous egg-shape predicted by most conventional yield functions for AZ31B, e.g., Plunkett et al. (2008) for this data set, or Yoon et al. (2014) for a similar data set. In general, it is specific to low order yield functions.

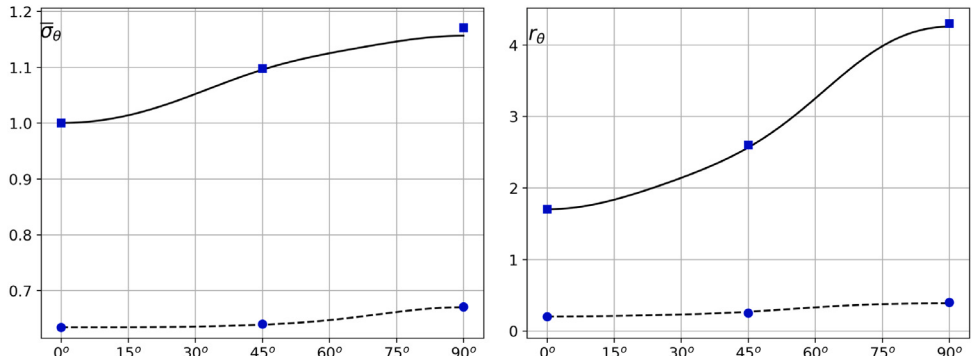


Fig. 7. AZ31B/Lou et al. (2007) ($n_Q = 4$): Predicted directional properties vs experiments (tension: continuous line; compression: dashed). Given the small number of parameters of SHY43, the quality of the fit in this case is surprisingly good. However, this is fortuitous, since SHY43 cannot fit the AZ31B data of Andar et al. (2012) with the same quality.

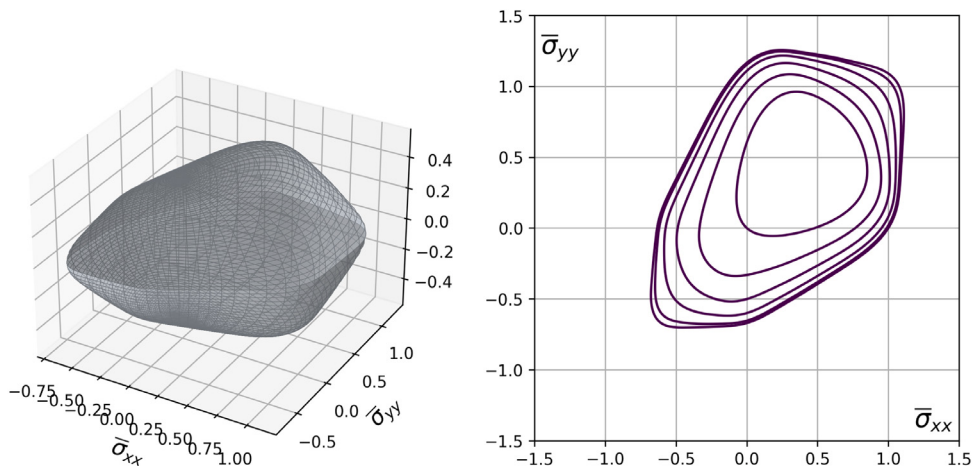


Fig. 8. AZ31B/Lou et al. (2007) ($n_Q = 14$): Predicted yield surface and several horizontal sections.

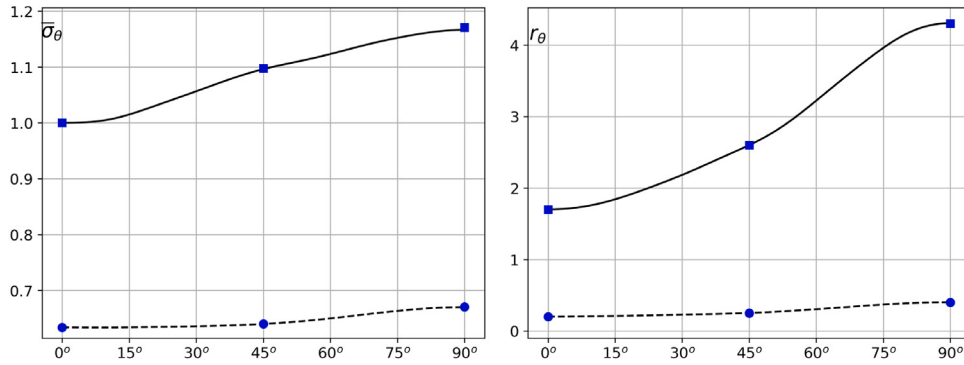


Fig. 9. AZ31B/Lou et al. (2007) ($n_Q = 14$): Predicted directional properties vs experiments (tension: continuous line; compression: dashed). In general, the best results for AZ31B are obtained with $n_Q = 16$. Nevertheless, practical applications may use lower degrees while retaining the main features of the yield surface. Here we used $n_Q = 14$ to demonstrate this point.

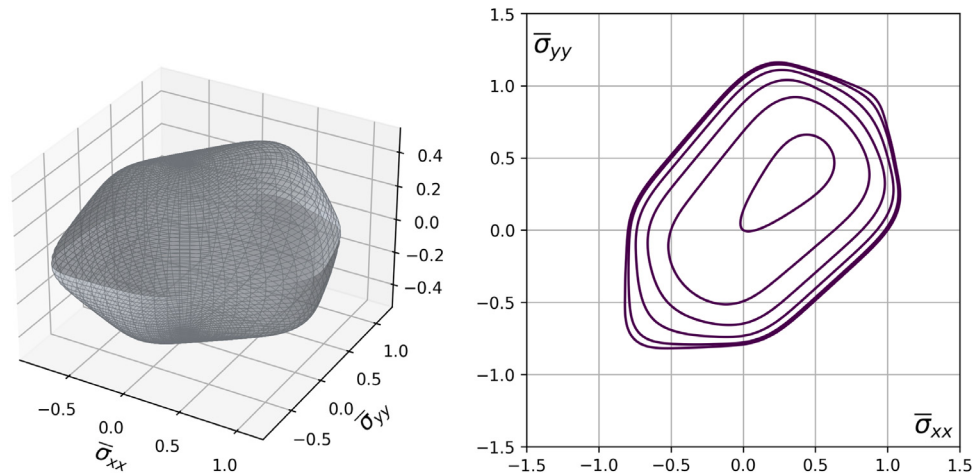


Fig. 10. AZ31B/Andar et al. (2012) ($n_Q = 14$): Predicted yield surface and several horizontal sections. Interestingly, the shape pattern here is quite different from that in Fig. 8. As explained in Section 8, this difference originates in the quite different tensile ratios of σ_{TD}/σ_{RD} featured by the samples of AZ31B investigated in the cited references.

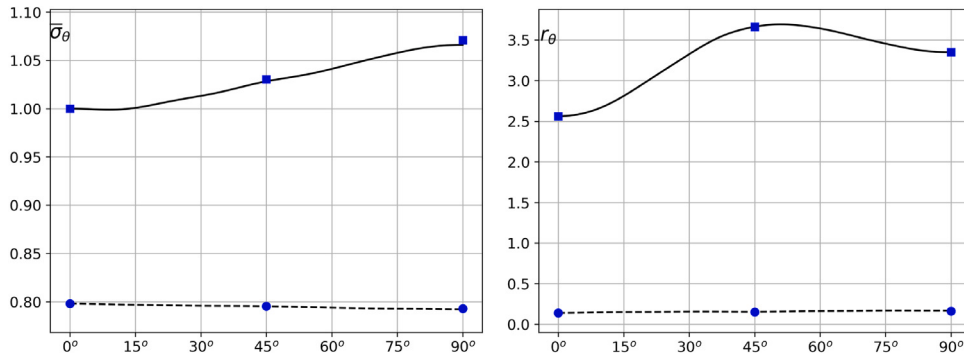


Fig. 11. AZ31B/Andar et al. (2012) ($n_Q = 14$): Predicted directional properties vs experiments (tension: continuous line; compression: dashed). The corresponding SHY43 model of this data set is reported in the files AZ31B_Andar2012_SHYqp_deg4_* at the GitHub repository; The quality of the fit is low, particularly for the tensile balanced-biaxial yielding point, and hence, in general, AZ31B is beyond the modeling range of SHY43.

The only meta-parameters that were varied in some of the examples featured in this section were the number of Bezier5YS shape parameters (and their values).

All models used a number of 19 plane sections for the general asymmetric case, and 15 for tension–compression symmetry to sample the Bezier5YS proto-model: With 30 points on each section, this amounts to 570 sampling locations in the general case. For all the models featured in this work, the lists of SHYqp material parameters (c_{P_i}, c_{Q_j}) can be found in the *_Err_and_Coeff.txt files at <https://github.com/stefanSCS/SHYqp> (together with the input files used to generate them).

Convexity was verified at a dense set of locations on the unit sphere comprised of all the points where convexity was enforced numerically and an additional set of approx. 7000 random points, as detailed in Appendix D. Two methods were employed: one based on the leading principal minors of the hessian matrix, and the other based on the Gaussian curvature, calculated for implicit functions by Eq. (137). The latter measure of convexity appears to be more stable numerically, being always positive when convexity is indeed achieved, whereas for the former measure, based on determinants, one has to accept as positive threshold negative numbers of the order of $-1.0e-10$.

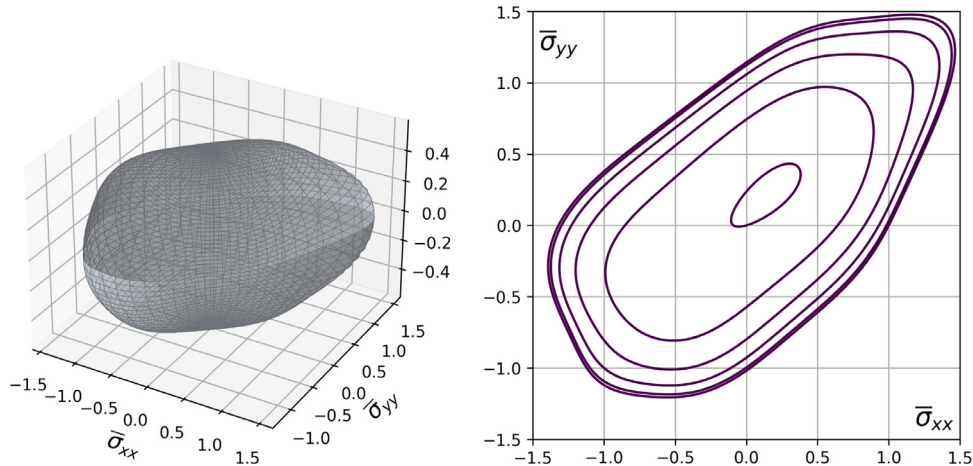


Fig. 12. Ti-CP/Raemy et al. (2017) ($n_Q = 10$): Predicted yield surface and several horizontal sections.

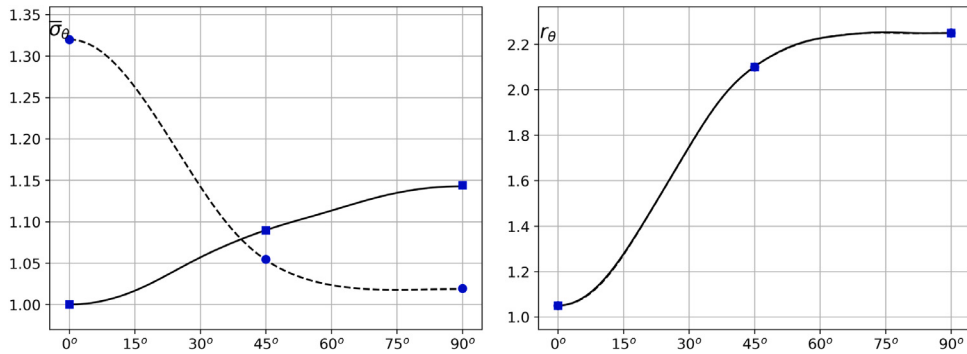


Fig. 13. Ti-CP/Raemy et al. (2017) ($n_Q = 10$): Predicted directional properties vs experiments (tension: continuous line; compression: dashed). The authors of the cited work mention that the r -values of the corresponding uniaxial compression tests could not be measured experimentally. An interesting numerical experiment is to assume complete symmetry in tension-compression for r -values: the figure (on the right) shows a perfect overlap of the two interpolations.

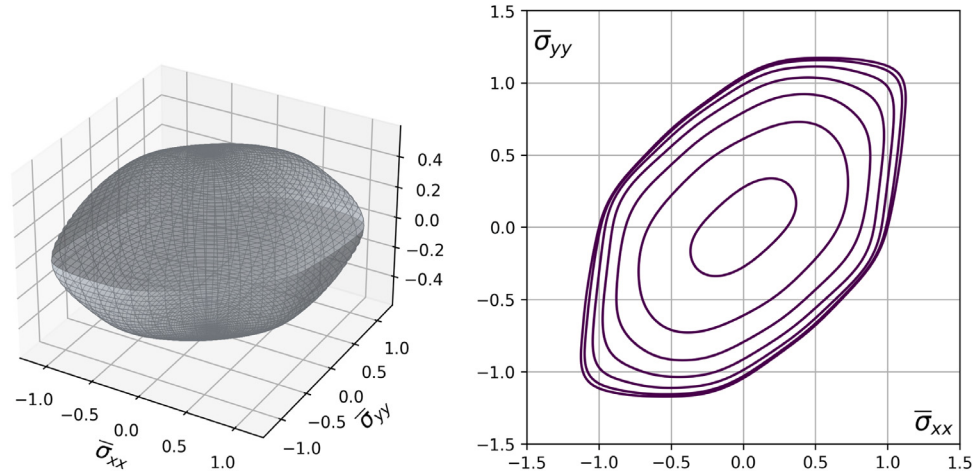


Fig. 14. AA5042-H2/Anon (2011) ($n_Q = 16$): Predicted yield surface and several horizontal sections. SHYqp with two shape parameters was used in this case with $s_1 = 0.7$ and $s_2 = 1$.

Finally, regarding the overall run-time required to obtain a solution, on an Intel-Xeon (3.20 GHz) workstation the following were typically observed: the low order SHYqp ($d n_Q \leq 10$) requires approx. 4 to 10s to complete, intermediary degrees $14 \leq n_Q \leq 20$ about 1-2 min, whereas for the max $n_Q = 24$ SHYqp requires about 5 min.

In order to associate a model with some numerical measure of success, we define the squared root error for stresses by

$$\Delta_{\Sigma} = \left[(\bar{\sigma}_{TB}^{exp} - \bar{\sigma}_{TB})^2 + (\bar{\sigma}_{CB}^{exp} - \bar{\sigma}_{CB})^2 + \sum_{\theta} (\bar{\sigma}_{T\theta}^{exp} - \bar{\sigma}_{T\theta})^2 + \sum_{\theta} (\bar{\sigma}_{C\theta}^{exp} - \bar{\sigma}_{C\theta})^2 \right]^{(1/2)} \quad (87)$$

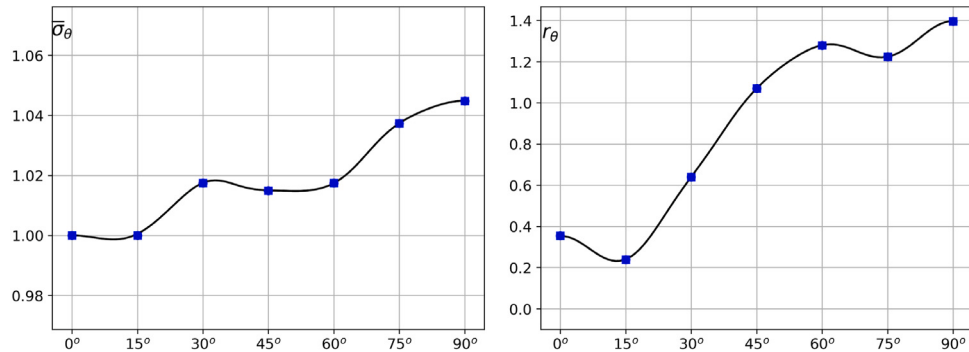


Fig. 15. AA5042-H2/Anon (2011) ($n_Q = 16$): Predicted directional properties vs experiments. This material is one of the most difficult benchmarks for yield functions, due to the high variation in directional properties and also to the unusually high (for aluminum alloys) balanced-biaxial yield stress.

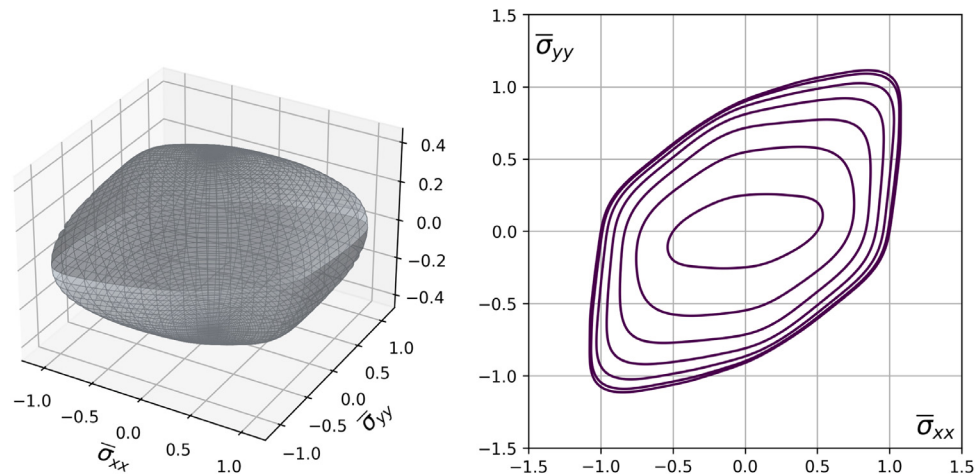


Fig. 16. AA2090-T3/Aretz and Barlat (2004) ($n_Q = 16$): Predicted yield surface and several horizontal sections. SHYqp with two shape parameters was used in this case with $s_1 = 0.7$ and $s_2 = 1$.

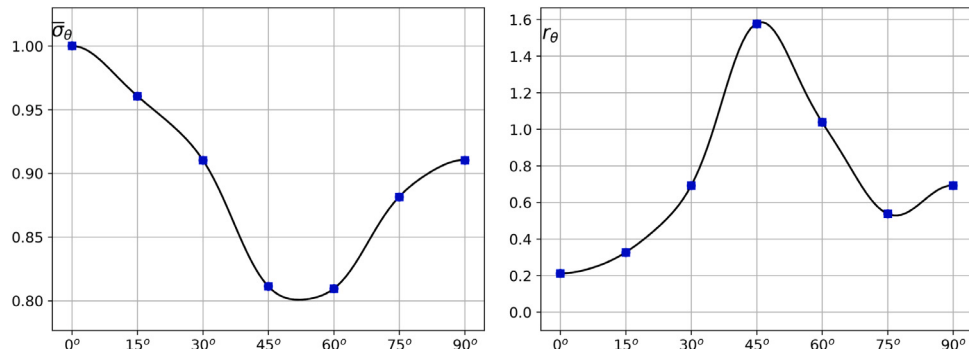


Fig. 17. AA2090-T3/Aretz and Barlat (2004) ($n_Q = 16$): Predicted directional properties vs experiments. Similar to AA5042-H2, this alloy also is a benchmark for yield functions, featuring an even higher variation in yield stresses. The model shown here appears to be almost perfect, see also the corresponding data in Table 1. Note, however, that even a model with a perfect fit of all directional data is not guaranteed to correctly predict the earing profile in cup-drawing experiments with this material, Soare and Barlat (2011), and additional input data may be required to model other features of its yield surface.

which is the Euclidean distance between all the normalized experimental stress data points $\bar{\sigma}^{exp}$ and predicted values $\bar{\sigma}$, including the balanced-biaxial points (which may actually be inferred from uniaxial data as explained in the section about Bezier5YS). Similarly, the overall measure of error for r -values is defined by

$$\Delta_R = \left[(r_{TB}^{exp} - r_{TB})^2 + (r_{CB}^{exp} - r_{CB})^2 + \sum_{\theta} (r_{T\theta}^{exp} - r_{T\theta})^2 + \sum_{\theta} (r_{C\theta}^{exp} - r_{C\theta})^2 \right]^{(1/2)} \quad (88)$$

Table 1 summarizes the performance of SHYqp for all the models featured in Figs. 6–19. All lattice classes are represented by applications to magnesium, titanium, aluminum and steel, with an emphasis on the HCP class. The references to tables in the ‘Data’ column are listed in Appendix E. Further comments are appended to figure captures where deemed necessary.

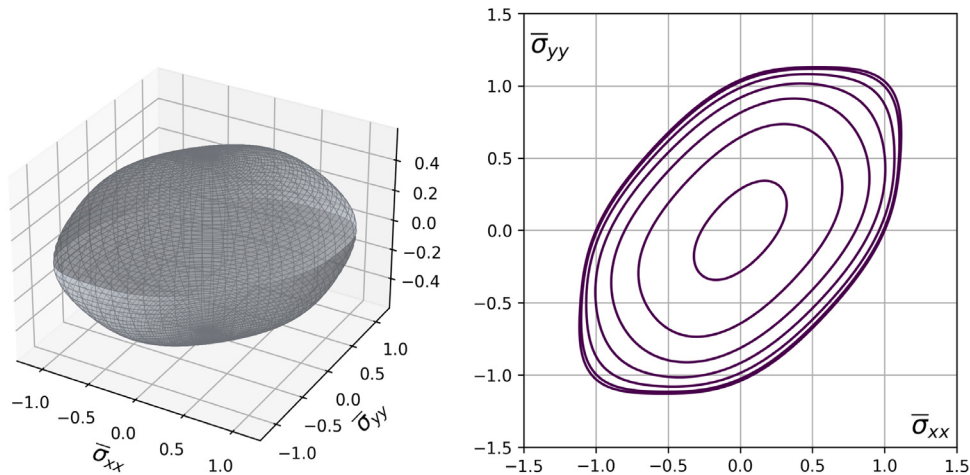


Fig. 18. DP980/Li et al. (2020) ($n_Q = 8$): Predicted yield surface and several horizontal sections. SHYqp with two shape parameters was used in this case with $s_1 = 0.5$ and $s_2 = 0.5$; In addition, the overall weight of the data was increased to $w^{(Y)} = 0.95$.

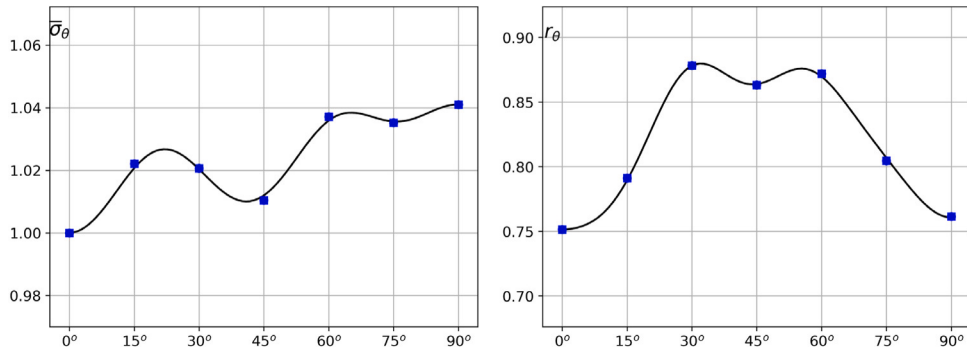


Fig. 19. DP980/Li et al. (2020) ($n_Q = 8$): Predicted directional properties vs experiments. For completeness, we show here the model of a dual phase steel. It is a member of the larger class of advanced high strength steels which are known to feature variations in mechanical properties among producers and even from batch to batch, Palaniswamy and Al-Nasser (2012). Hence a fast and accurate modeling procedure for their properties is essential in production.

8. Further investigations into the yield surface shape of AZ31B

The SHYqp models of AZ31B featured so far were constructed using two quite strong assumptions upon their input data: The corresponding Bezier5YS proto-models had only one shape parameter and the balanced-biaxial data (when not available) was estimated via Eq. (48). Here the matter is reconsidered by employing crystal plasticity calculations to obtain more rigorous estimates of the yielding properties of AZ31B. For this purpose, a distribution of 2607 grain orientations was generated based on the pole figures reported in Fig. 14(a) of Lou et al. (2007) and the crystal plasticity simulation kit Damask/Grid, Roters et al. (2019), was employed to estimate the overall response of a cube shaped representative volume element (RVE) of size $10 \times 10 \times 10 \mu\text{m}^3$. The texture and the RVE employed are shown in Fig. 20, while the corresponding data files (grain orientations and geometry) can be accessed at SHYqp' GitHub.

Since only the initial stages of yielding are of interest here, the crystal plasticity parameters were identified based on the RD tension and compression loading curves reported in Fig. 6(a) of Lou et al. (2007) for strains up to 0.02; Also, since a definitive methodology for the specification of the deformation modes of Mg-crystals is not yet established, e.g., Agnew and Duygulu (2005), Graf et al. (2007), Zecevic et al. (2018), we took a pragmatic approach and used the three most commonly employed slip families, i.e., basal, prismatic, pyramidal- $\langle a \rangle$, pyramidal- $\langle c+a \rangle$ -II, and the extension twin as main parameters for the SciPy's implementation of the Nelder–Mead optimization algorithm (with the parameters reported in Table 7 of Roters et al. (2019) as initial guess) to obtain a first rough estimate, which was then refined

by trial-and-error. The final parameters are reported in Table 2 and the corresponding predicted loading curves are shown in Fig. 21.

Overall, the results in Fig. 21 show that the synthetic texture employed to construct the RVE does capture the main features of the experimental data reported in Lou et al. (2007). The same RVE was then tested along several constant stress ratio radial loading paths, spanning all four quadrants of the biaxial $(\sigma_{xx}, \sigma_{yy})$ plane, and the corresponding yielding points were estimated based on the accumulated plastic work, Hill and Hutchinson (1992), with the threshold value corresponding to 0.2% plastic strain along RD. The result of these calculations is shown in Fig. 22/Left together with the biaxial curves of three SHYqp models:

- model-A constructed using Bezier5YS with one shape parameter ($s = 1$) and the Damask calculated balanced-biaxial points
- model-B constructed using Bezier5YS with four shape parameters ($s_1 = 0.5, s_2 = s_3 = s_4 = 1$) and the Damask calculated balanced-biaxial points
- model-C constructed using Bezier5YS with four shape parameters ($s_1 = 0.5, s_2 = s_3 = s_4 = 1$) and with all the Damask calculated biaxial points added to the input data for the optimization of the SHYqp parameters.

Table 2

Single crystal parameters for magnesium sheet AZ31B. Notation from Sections 6.2.2 and 7.8/Table.6 of Roters et al. (2019). Elastic constants and the last column below are the same as in the cited reference. All entries of the latent hardening matrices were taken equal to 1. Only the first six columns below were subject to optimization. All parameters are in MPa units. Cells where data is ‘not applicable’ are marked with *.

	Basal	Prism	Pyr<a>	Pyr<c+a>-II	Ext.Twin	$h_0^{s-s} = 500$	$n = 20$
ξ_0	20	85	115	115	40	$h_0^{w-tw} = 10$	$\dot{\gamma}_0^s = 0.001$
ξ_∞	21	400	300	300	*	$h_0^{w-s} = 50$	$\dot{\gamma}_0^{tw} = 0.001$

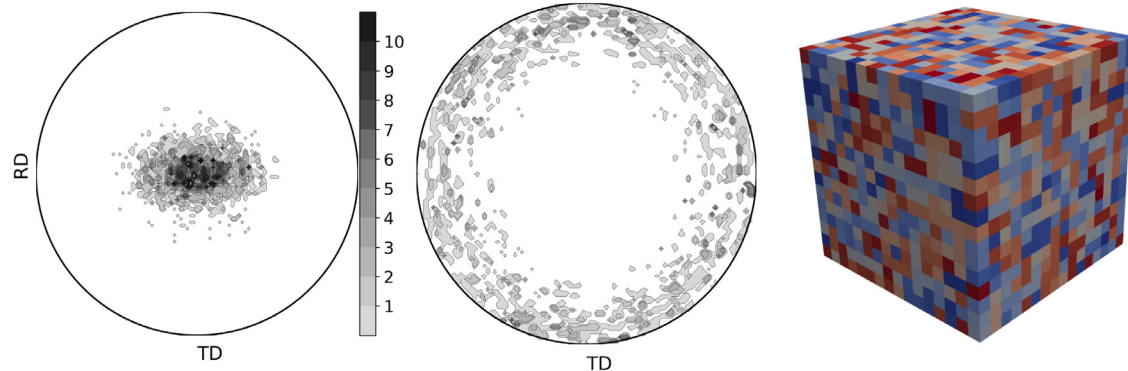


Fig. 20. AZ31B simulated texture: (0001) and (10̄10) pole figures; RVE geometry generated with Damask using a $16 \times 16 \times 16$ grid on each grain; RVE cube image visualized with ParaView (<https://www.paraview.org>). The pole figures densities are normalized by a reference density corresponding to a set of 5144 equal area bins generated by an approach similar to that described in Appendix D.

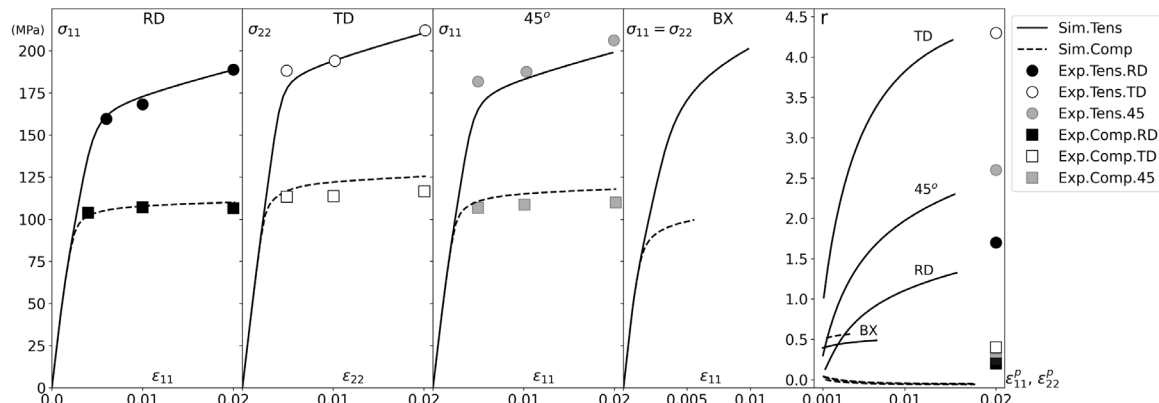


Fig. 21. Fit of the RD tension and compression loading curves and predictions for TD, 45° and balanced-biaxial (BX); Loading curves experimental data digitized from Fig. 6(a) of Lou et al. (2007). Last figure in the sequence shows fitted (for RD) and predicted r-values; The experimental r-values are the stabilized (long-range) data reported in the cited article.

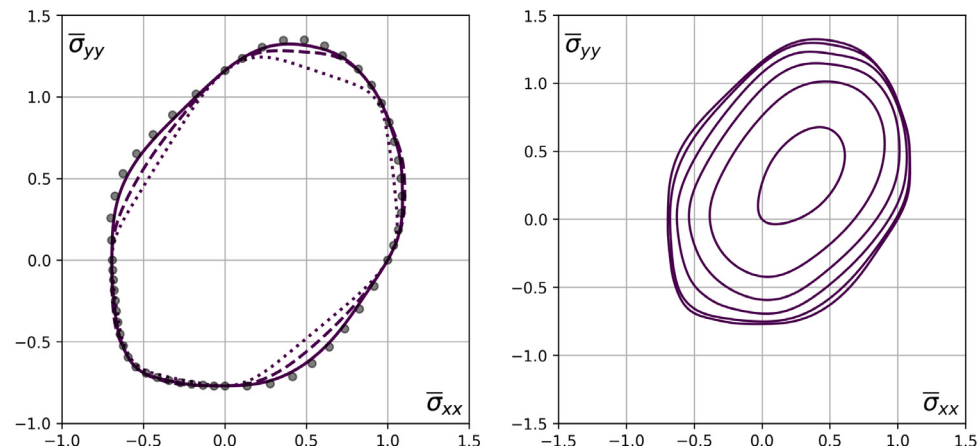


Fig. 22. AZ31B/Lou et al. (2007) ($n_Q = 14$): Yield surface at 0.2% plastic deformation. **Left:** Biaxial yielding points (shown as grey circles) estimated with Damask and $\sigma_{xy} = 0$ contours of three SHYqp models: Model-A(dotted), Model-B(dashed), Model-C(continuous line). **Right:** Several $\sigma_{xy} = c\tau$ contours of the SHYqp Model-C.

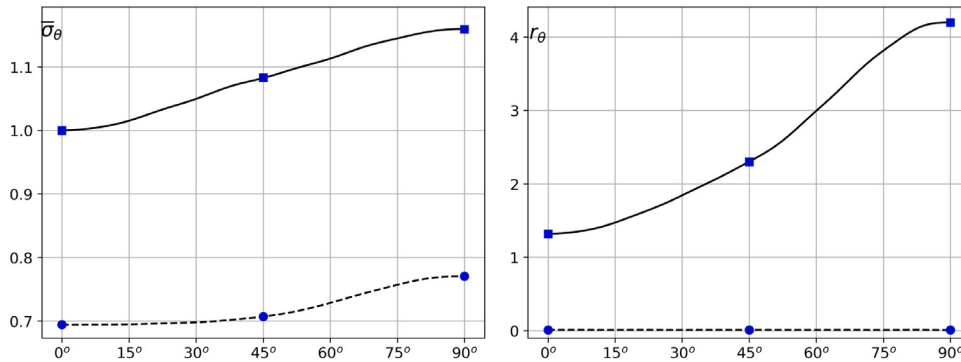


Fig. 23. AZ31B/Lou et al. (2007) ($n_Q = 14$): Directional properties of the SHYqp Model-C (tensile properties are shown with continuous line, while dashed represents compression). Note: The Damask simulations estimate very small, yet negative r -values for the uniaxial compression tests. Since the current implementation of SHYqp allows only positive values for its input data, all three models were constructed with input $r_C(\theta) = 0.01$ for $\theta \in \{0^\circ, 45^\circ, 90^\circ\}$.

Model-C, further detailed in Fig. 22/Right and Fig. 23, provides the most accurate fitting of the entire set of calculated biaxial yielding points; Model-B achieves similar results in the first and third quadrants but underestimates the yielding threshold in the second and fourth quadrants (these two quadrants are significant for sheet drawing operations, where a material element is subject to tensile stresses in the draw direction and an in-plane perpendicular compression); Model-A has the highest deviation from the biaxial data set, being representative of the minimal curvature SHYqp models of AZ31B shown in the previous section. The yield surface shapes in Soare and Benzerga (2016) are similar to Model-A.

The results in Fig. 22 show that the biaxial yielding curve of AZ31B features significant shape variations between the first and the fourth quadrants. This is a consequence of the different deformation mechanisms activated at crystal level in the loading regimes corresponding to each quadrant. The yield surfaces of Steglich et al. (2016) and Kondori et al. (2019) are of the kind represented by Model-B. The cited references employ a two surface yielding model to capture the difference between the deformation mechanisms of magnesium crystals in tension and compression (at the expense of introducing a gradient discontinuity in the second and fourth pure shear quadrants). Here the shape parameters of Bezier5YS play a similar role, yet in finer and more localized detail. This can be further illustrated by reconsidering the AZ31B data set of Andar et al. (2012), where experimental biaxial data in the first quadrant is reported. Figs. 24 and 25 show the corresponding SHYqp models A, B and C of this data set, constructed with shape parameters $s = 1$, and $s_1 = 0.1$, $s_2 = s_3 = s_4 = 1$, respectively. Both Fig. 22/Left and Fig. 24/Left show the same overall trend: improvement from Model-A to Model-C by the use of four shape parameters. Noteworthy, the difference between Models B and C in the latter case is smaller (almost negligible). This is expected to hold even if additional data in the second and fourth quadrants were accounted for. The reason for this is that the samples studied by Andar et al. (2012) feature a smaller difference between tensile RD and TD yielding properties (being quite close to transversely isotropic): $(\sigma_{TD} - \sigma_{RD})/\sigma_{RD} \approx 7.1\%$. In the case of the samples studied by Lou et al. (2007), the difference is about 15.9%, which correlates well with the higher concentration of grain c -axes along RD, as featured in the (0001)-pole figure in Fig. 20.

9. Further discussion: line search and Horner scheme in FEA implementation

The applications shown in the previous sections demonstrate the modeling power of the combined Bezier5YS-SHYqp framework. It matches or surpasses the modeling capabilities of virtually any state of the art yield criterion, it can be adapted to incorporate any experimental data set, and, perhaps most importantly, it is a powerful data

analysis tool with the capability to bring new insights into the data itself.

Given a minimal experimental dataset, Bezier5YS generates a complete plane stress yield surface model based only on geometrical considerations, a proto-model that matches exactly the directional data. SHYqp provides an analytical formula. An important feature of SHYqp, originating in its harmonic *polynomial* formulation, is that all gradient and hessian calculations are analytic, which makes it attractive for finite element implementation. For the minimal polynomial degree, $n_Q = 4$, SHYqp should achieve run-times close to the classical Hill48 quadratic without additional precautions regarding the convergence of the return mapping algorithm and/or the optimal evaluation of the function, gradient and hessian. However, for higher degrees, $n_Q \geq 6$, two issues become significant:

- Proper convergence of the return mapping algorithm: The yield surface shapes of aluminum and magnesium alloys feature vertices near which the underlying Newton–Raphson iterations may not converge with precision to the correct stress state.
- The number of multiplications in the canonical polynomial formulation of SHYqp grows rapidly with the degree n_Q , with a heavy impact on the overall run-time of a simulation and numerical stability.

The solution to the first issue is straightforward and well-known, e.g., Bonet and Wood (1997): No Newton without line search. This is because taking the full Newton-step may fail even when solving one dimensional non-linear equations. A quadratic line search as used in Seifert and Schmidt (2008) and Soare and Barlat (2011) appears to be sufficient: It has a relatively small impact on the overall computational effort while ensuring the sought-for accuracy.

The solution to the second issue is to employ an optimized evaluation of all polynomial expressions (including gradient and hessian) via a Horner scheme. The Horner scheme is well-known for polynomials of one argument but there is no known general Horner scheme for multi-dimensional polynomials. Fortunately, for the case of orthotropic homogeneous polynomials such an optimal (Horner) evaluation scheme can indeed be formulated. To simplify the presentation we shall consider only the particular case when $n_Q = 8$ but the algorithm is obviously applicable to any degree (even or odd). In particular, the same considerations apply to the sixth order polynomial Poly6 considered by Tong (2018) and Soare (2022), and further to any high order homogeneous polynomial formulation.

To simplify notation, we substitute x, y and z for σ_{xx}, σ_{yy} and σ_{xy} , respectively, and write the Q -part of SHYqp in the form

$$\begin{aligned} Q &= P_8 + P_6 z^2 + P_4 z^4 + P_2 z^6 + a_0^0 z^8 \\ &= P_8 + z^2 (P_6 + z^2 (P_4 + z^2 (P_2 + z^2 P_0))) \end{aligned} \quad (89)$$

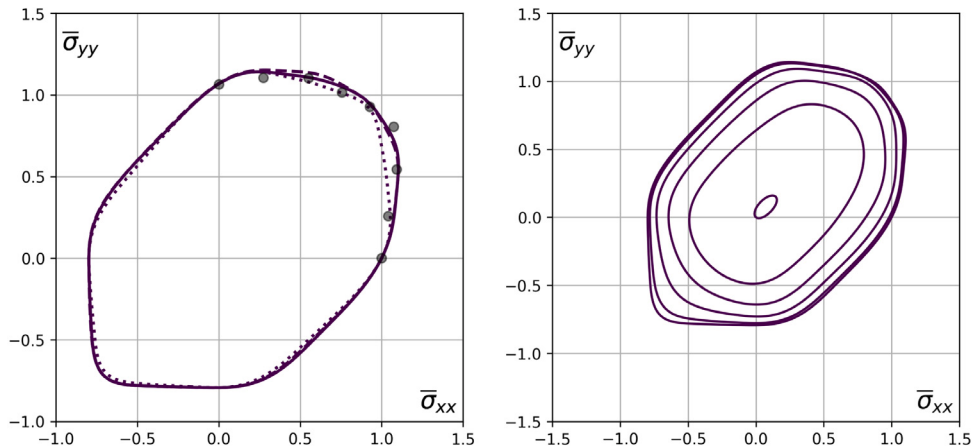


Fig. 24. AZ31B/Andar et al. (2012) ($n_Q = 14$): Yield surface at 0.2% plastic deformation. **Left.** Experimental biaxial yielding points (shown as grey circles) digitized from the cited reference, and $\sigma_{xy} = 0$ contours of three SHYqp models: Model-A (dotted), Model-B (dashed), Model-C (continuous line). **Right.** Several $\sigma_{xy} = ct$ contours of the SHYqp Model-C.

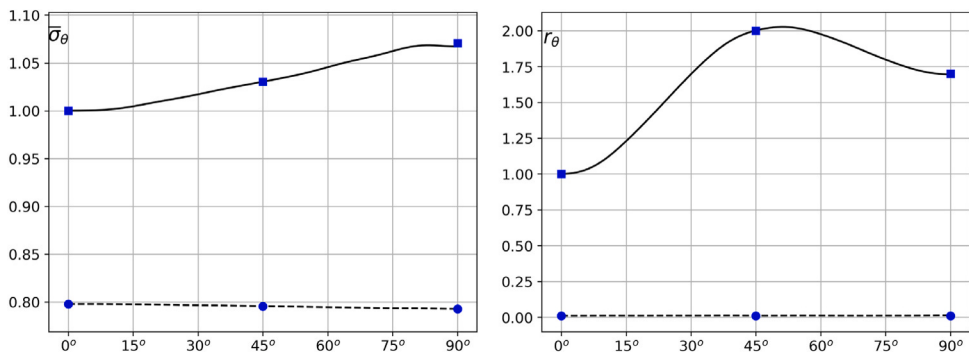


Fig. 25. AZ31B/Andar et al. (2012) ($n_Q = 14$): Directional properties of the SHYqp Model-C (tensile properties are shown with continuous line, while dashed represents compression). Note: Based on the previous Damask simulations, the r -values in compression in the initial yielding stages are expected to be close to zero and hence all three models were constructed with input $r_C(\theta) = 0.01$ for $\theta \in \{0^\circ, 45^\circ, 90^\circ\}$.

The second equality represents the first level of the Horner-based evaluation of Q . Here a_0^0 corresponds to the 25-th coefficient of Q and, in general

$$P_k(x, y) = \sum_{i=0}^k a_i^k x^{k-i} y^i, \quad k = 0, 1, 2, 3, \dots, 8 \quad (90)$$

with a_i^k denoting the i th coefficient of P_k . Then the second, deeper level of evaluation optimization is based on the observation that

$$P_k = x P_{k-1} + a_k^k y^k \quad (91)$$

Then assuming the vector of powers of y is calculated in advance and stored as

$$(Y_i)_i = (1, y, y^2, y^3, y^4, y^5, y^6, y^7, y^8) \quad (92)$$

the calculation of each of the polynomials P_k in Eq. (89) proceeds as follow:

$$P_2 = x P_1 + a_2^2 Y_2 \quad (93)$$

$$P_4 = x (x P_1 + a_2^4 Y_2) + a_3^4 Y_3 + a_4^4 Y_4 \quad (94)$$

etc.

Declaration of competing interest

The authors declare that they have no known competing financial interests or personal relationships that could have appeared to influence the work reported in this paper.

Data availability

Data supporting this study are included within the article and/or supporting materials

Appendix A. Gradient calculations

For a function $f = f(\sigma) = \hat{f}(s)$, with $s \in \mathbb{S}$, its gradient is calculated according to the formulas in Eqs. (15) and (16) which are recalled here for convenience:

$$\begin{aligned} \frac{\partial f}{\partial \sigma_{11}} &= \sqrt{\frac{2}{3}} \frac{\partial \hat{f}}{\partial s_1}, \quad \frac{\partial f}{\partial \sigma_{22}} = \frac{1}{\sqrt{2}} \frac{\partial \hat{f}}{\partial s_2} - \frac{1}{\sqrt{6}} \frac{\partial \hat{f}}{\partial s_1}, \\ \frac{\partial f}{\partial \sigma_{33}} &= - \left(\frac{1}{\sqrt{6}} \frac{\partial \hat{f}}{\partial s_1} + \frac{1}{\sqrt{2}} \frac{\partial \hat{f}}{\partial s_2} \right) \end{aligned} \quad (95)$$

$$\frac{\partial f}{\partial \sigma_{12}} = \frac{1}{\sqrt{2}} \frac{\partial \hat{f}}{\partial s_3}, \quad \frac{\partial f}{\partial \sigma_{13}} = \frac{1}{\sqrt{2}} \frac{\partial \hat{f}}{\partial s_4}, \quad \frac{\partial f}{\partial \sigma_{23}} = \frac{1}{\sqrt{2}} \frac{\partial \hat{f}}{\partial s_5} \quad (96)$$

In this study, the function \hat{f} has the specific form

$$\hat{f}(s) = \sqrt{\frac{3}{2}} |s| [1 + P(\mathbf{u}) + Q(\mathbf{u})] \quad (97)$$

with $\mathbf{u} = s/|s|$ and P and Q homogeneous polynomials of degrees $2m-1$ and $2m$, respectively. We recall that a homogeneous polynomial R_n of degree n satisfies:

$$R_n(\mathbf{u}) = \frac{1}{|s|^n} R_n(s), \quad \frac{\partial R_n}{\partial s_k}(\mathbf{u}) = \frac{1}{|s|^{n-1}} \frac{\partial R_n}{\partial s_k}(s) \quad (98)$$

Then starting from the basic formula

$$\frac{\partial|s|}{\partial s_k} = \frac{s_k}{|s|}$$

the components of the gradient of \hat{f} in Eq. (97) are:

$$\frac{\partial \hat{f}}{\partial s_k}(s) = \sqrt{\frac{3}{2}} \left\{ \frac{s_k}{|s|} [1 + P(\mathbf{u}) + Q(\mathbf{u})] + |s| \left[\frac{d}{ds_k} P(\mathbf{u}) + \frac{d}{ds_k} Q(\mathbf{u}) \right] \right\} \quad (99)$$

Using Eq. (98) with $n = n_P$, the derivatives of P are calculated as follow:

$$\begin{aligned} \frac{d}{ds_k} P(\mathbf{u}) &= \frac{d}{ds_k} \left(\frac{1}{|s|^{n_P}} \right) P(s) + \frac{1}{|s|^{n_P}} \frac{\partial P}{\partial s_k}(s) \\ &= \frac{-n_P}{|s|^{n_P+1}} \frac{s_k}{|s|} P(s) + \frac{1}{|s|^{n_P}} \frac{\partial P}{\partial s_k}(s) \\ &= \frac{-n_P s_k}{|s|^2} P(\mathbf{u}) + \frac{1}{|s|} \frac{\partial P}{\partial s_k}(\mathbf{u}) \end{aligned}$$

With a similar formula holding for Q , substituting back into Eq. (99) obtains:

$$\frac{\partial \hat{f}}{\partial s_k}(s) = \sqrt{\frac{3}{2}} \left\{ u_k [1 - (n_P - 1)P(\mathbf{u}) - (n_Q - 1)Q(\mathbf{u})] + \frac{\partial P}{\partial s_k}(\mathbf{u}) + \frac{\partial Q}{\partial s_k}(\mathbf{u}) \right\} \quad (100)$$

Eqs. (95), (96) and (100) provide the recipe for calculating the gradient of the yield function defined by Eq. (97). In Eq. (100), $\partial P/\partial s_k$ and $\partial Q/\partial s_k$ are normal partial derivatives of the respective polynomials.

We close with a note on the nature of the derivatives in Eqs. (95) and (96): These are tensor components (i.e., derivatives with respect to the basis of $\mathbb{R}^3 \times \mathbb{R}^3 \approx \mathbb{R}^9$).

Appendix B. Hessian calculations

To calculate the Hessian matrix of the yield function one could follow the pattern established by Eq. (14). Since the yield function f admits two representations, one as $f : \mathbb{R}^9 \rightarrow \mathbb{R}$ and another as $\hat{f} : \mathbb{S} \rightarrow \mathbb{R}$, which coincide on \mathbb{S} , a subspace of \mathbb{R}^9 , there must hold:

$$\mathbf{H} = D^2 f = \frac{\partial^2 f}{\partial \sigma_{ij} \partial \sigma_{kl}} \mathbf{e}_i \otimes \mathbf{e}_j \otimes \mathbf{e}_k \otimes \mathbf{e}_l = \frac{\partial^2 \hat{f}}{\partial s_p \partial s_q} \mathbf{g}_p \otimes \mathbf{g}_q \quad (101)$$

Expanding the tensor products $\mathbf{g}_p \otimes \mathbf{g}_q$ by using Eqs. (4)–(6), and then identifying the corresponding terms in the above formula obtains the desired second order derivatives. A more direct approach, the one followed here, is to employ directly the formulas in Eqs. (15)–(16), the symmetry of the mixed second order partial derivatives and the pressure independence of f . Then, using Voigt's notation for reduced indices:

$$\begin{aligned} H_{11} &= \frac{\partial^2 f}{\partial \sigma_{11} \partial \sigma_{11}} = \frac{2}{\sqrt{6}} \frac{\partial}{\partial s_1} \left(\frac{2}{\sqrt{6}} \frac{\partial \hat{f}}{\partial s_1} \right) \\ &= \frac{2}{3} \frac{\partial^2 \hat{f}}{\partial s_1 \partial s_1} \end{aligned} \quad (102)$$

$$\begin{aligned} H_{12} &= \frac{\partial^2 f}{\partial \sigma_{11} \partial \sigma_{22}} = \frac{-1}{\sqrt{6}} \frac{\partial}{\partial s_1} \left(\frac{2}{\sqrt{6}} \frac{\partial \hat{f}}{\partial s_1} \right) + \frac{1}{\sqrt{2}} \frac{\partial}{\partial s_2} \left(\frac{2}{\sqrt{6}} \frac{\partial \hat{f}}{\partial s_1} \right) \\ &= \frac{-1}{3} \frac{\partial^2 \hat{f}}{\partial s_1 \partial s_1} + \frac{1}{\sqrt{3}} \frac{\partial^2 \hat{f}}{\partial s_1 \partial s_2} \end{aligned} \quad (103)$$

$$H_{13} = \frac{\partial^2 f}{\partial \sigma_{11} \partial \sigma_{33}} = -\frac{\partial^2 f}{\partial \sigma_{11} \partial \sigma_{11}} - \frac{\partial^2 f}{\partial \sigma_{11} \partial \sigma_{22}} = -(H_{11} + H_{12}) \quad (104)$$

$$H_{14} = \frac{\partial^2 f}{\partial \sigma_{11} \partial \sigma_{12}} = \frac{1}{\sqrt{2}} \frac{\partial}{\partial s_3} \left(\frac{2}{\sqrt{6}} \frac{\partial \hat{f}}{\partial s_1} \right) = \frac{1}{\sqrt{3}} \frac{\partial^2 \hat{f}}{\partial s_1 \partial s_3} \quad (105)$$

$$H_{15} = \frac{\partial^2 f}{\partial \sigma_{11} \partial \sigma_{13}} = \frac{1}{\sqrt{2}} \frac{\partial}{\partial s_4} \left(\frac{2}{\sqrt{6}} \frac{\partial \hat{f}}{\partial s_1} \right) = \frac{1}{\sqrt{3}} \frac{\partial^2 \hat{f}}{\partial s_1 \partial s_4} \quad (106)$$

$$H_{16} = \frac{\partial^2 f}{\partial \sigma_{11} \partial \sigma_{23}} = \frac{1}{\sqrt{2}} \frac{\partial}{\partial s_5} \left(\frac{2}{\sqrt{6}} \frac{\partial \hat{f}}{\partial s_1} \right) = \frac{1}{\sqrt{3}} \frac{\partial^2 \hat{f}}{\partial s_1 \partial s_5} \quad (107)$$

$$\begin{aligned} H_{22} &= \frac{\partial^2 f}{\partial \sigma_{22} \partial \sigma_{22}} = \left(\frac{-1}{\sqrt{6}} \frac{\partial}{\partial s_1} + \frac{1}{\sqrt{2}} \frac{\partial}{\partial s_2} \right) \left(\frac{-1}{\sqrt{6}} \frac{\partial \hat{f}}{\partial s_1} + \frac{1}{\sqrt{2}} \frac{\partial \hat{f}}{\partial s_2} \right) \\ &= \frac{1}{6} \frac{\partial^2 \hat{f}}{\partial s_1 \partial s_1} + \frac{-1}{\sqrt{3}} \frac{\partial^2 \hat{f}}{\partial s_1 \partial s_2} + \frac{1}{2} \frac{\partial^2 \hat{f}}{\partial s_2 \partial s_2} \end{aligned} \quad (108)$$

$$H_{23} = \frac{\partial^2 f}{\partial \sigma_{22} \partial \sigma_{33}} = -\frac{\partial^2 f}{\partial \sigma_{11} \partial \sigma_{22}} - \frac{\partial^2 f}{\partial \sigma_{22} \partial \sigma_{22}} = -(H_{21} + H_{22}) \quad (109)$$

$$\begin{aligned} H_{24} &= \frac{\partial^2 f}{\partial \sigma_{22} \partial \sigma_{12}} = \frac{1}{\sqrt{2}} \frac{\partial}{\partial s_3} \left(\frac{-1}{\sqrt{6}} \frac{\partial \hat{f}}{\partial s_1} + \frac{1}{\sqrt{2}} \frac{\partial \hat{f}}{\partial s_2} \right) \\ &= \frac{-1}{2\sqrt{3}} \frac{\partial^2 \hat{f}}{\partial s_1 \partial s_3} + \frac{1}{2} \frac{\partial^2 \hat{f}}{\partial s_2 \partial s_3} \end{aligned} \quad (110)$$

$$\begin{aligned} H_{25} &= \frac{\partial^2 f}{\partial \sigma_{22} \partial \sigma_{13}} = \frac{1}{\sqrt{2}} \frac{\partial}{\partial s_4} \left(\frac{-1}{\sqrt{6}} \frac{\partial \hat{f}}{\partial s_1} + \frac{1}{\sqrt{2}} \frac{\partial \hat{f}}{\partial s_2} \right) \\ &= \frac{-1}{2\sqrt{3}} \frac{\partial^2 \hat{f}}{\partial s_1 \partial s_4} + \frac{1}{2} \frac{\partial^2 \hat{f}}{\partial s_2 \partial s_4} \end{aligned} \quad (111)$$

$$\begin{aligned} H_{26} &= \frac{\partial^2 f}{\partial \sigma_{22} \partial \sigma_{23}} = \frac{1}{\sqrt{2}} \frac{\partial}{\partial s_5} \left(\frac{-1}{\sqrt{6}} \frac{\partial \hat{f}}{\partial s_1} + \frac{1}{\sqrt{2}} \frac{\partial \hat{f}}{\partial s_2} \right) \\ &= \frac{-1}{2\sqrt{3}} \frac{\partial^2 \hat{f}}{\partial s_1 \partial s_5} + \frac{1}{2} \frac{\partial^2 \hat{f}}{\partial s_2 \partial s_5} \end{aligned} \quad (112)$$

$$H_{33} = \frac{\partial^2 f}{\partial \sigma_{33} \partial \sigma_{33}} = -\frac{\partial^2 f}{\partial \sigma_{11} \partial \sigma_{33}} - \frac{\partial^2 f}{\partial \sigma_{22} \partial \sigma_{33}} = -(H_{31} + H_{32}) \quad (113)$$

$$H_{34} = \frac{\partial^2 f}{\partial \sigma_{33} \partial \sigma_{12}} = -\frac{\partial^2 f}{\partial \sigma_{11} \partial \sigma_{12}} - \frac{\partial^2 f}{\partial \sigma_{22} \partial \sigma_{12}} = -(H_{14} + H_{24}) \quad (114)$$

$$H_{35} = \frac{\partial^2 f}{\partial \sigma_{33} \partial \sigma_{13}} = -\frac{\partial^2 f}{\partial \sigma_{11} \partial \sigma_{13}} - \frac{\partial^2 f}{\partial \sigma_{22} \partial \sigma_{13}} = -(H_{15} + H_{25}) \quad (115)$$

$$H_{36} = \frac{\partial^2 f}{\partial \sigma_{33} \partial \sigma_{23}} = -\frac{\partial^2 f}{\partial \sigma_{11} \partial \sigma_{23}} - \frac{\partial^2 f}{\partial \sigma_{22} \partial \sigma_{23}} = -(H_{16} + H_{26}) \quad (116)$$

$$H_{44} = \frac{\partial^2 f}{\partial \sigma_{12} \partial \sigma_{12}} = \frac{1}{\sqrt{2}} \frac{\partial}{\partial s_3} \left(\frac{1}{\sqrt{2}} \frac{\partial \hat{f}}{\partial s_3} \right) = \frac{1}{2} \frac{\partial^2 \hat{f}}{\partial s_3 \partial s_3} \quad (117)$$

$$H_{45} = \frac{\partial^2 f}{\partial \sigma_{12} \partial \sigma_{13}} = \frac{1}{\sqrt{2}} \frac{\partial}{\partial s_4} \left(\frac{1}{\sqrt{2}} \frac{\partial \hat{f}}{\partial s_3} \right) = \frac{1}{2} \frac{\partial^2 \hat{f}}{\partial s_3 \partial s_4} \quad (118)$$

$$H_{46} = \frac{\partial^2 f}{\partial \sigma_{12} \partial \sigma_{23}} = \frac{1}{\sqrt{2}} \frac{\partial}{\partial s_5} \left(\frac{1}{\sqrt{2}} \frac{\partial \hat{f}}{\partial s_3} \right) = \frac{1}{2} \frac{\partial^2 \hat{f}}{\partial s_3 \partial s_5} \quad (119)$$

$$H_{55} = \frac{\partial^2 f}{\partial \sigma_{13} \partial \sigma_{13}} = \frac{1}{\sqrt{2}} \frac{\partial}{\partial s_4} \left(\frac{1}{\sqrt{2}} \frac{\partial \hat{f}}{\partial s_4} \right) = \frac{1}{2} \frac{\partial^2 \hat{f}}{\partial s_4 \partial s_4} \quad (120)$$

$$H_{56} = \frac{\partial^2 f}{\partial \sigma_{13} \partial \sigma_{23}} = \frac{1}{\sqrt{2}} \frac{\partial}{\partial s_5} \left(\frac{1}{\sqrt{2}} \frac{\partial \hat{f}}{\partial s_4} \right) = \frac{1}{2} \frac{\partial^2 \hat{f}}{\partial s_4 \partial s_5} \quad (121)$$

$$H_{66} = \frac{\partial^2 f}{\partial \sigma_{23} \partial \sigma_{23}} = \frac{1}{\sqrt{2}} \frac{\partial}{\partial s_5} \left(\frac{1}{\sqrt{2}} \frac{\partial \hat{f}}{\partial s_5} \right) = \frac{1}{2} \frac{\partial^2 \hat{f}}{\partial s_5 \partial s_5} \quad (122)$$

The second order derivatives of \hat{f} are calculated by using Eq. (100) together with the homogeneity of P and Q :

$$\frac{\partial^2 \hat{f}}{\partial s_k \partial s_l} = \sqrt{\frac{3}{2}} \frac{\partial}{\partial s_l} \left\{ \frac{s_k}{|s|} \left[1 - (n_P - 1) \frac{P(s)}{|s|^{n_P}} - (n_Q - 1) \frac{Q(s)}{|s|^{n_Q}} \right] \right\}$$

$$\begin{aligned}
& + \frac{1}{|s|^{n_P-1}} \frac{\partial P}{\partial s_k}(s) + \frac{1}{|s|^{n_Q-1}} \frac{\partial Q}{\partial s_k}(s) \Big\} \\
= & \sqrt{\frac{3}{2}} \frac{1}{|s|} \left\{ (\delta_{kl} - u_k u_l) [1 - (n_P - 1) P(\mathbf{u}) - (n_Q - 1) Q(\mathbf{u})] \right. \\
& + \sqrt{\frac{3}{2}} \frac{u_k}{|s|} \left[n_P(n_P - 1) u_l P(\mathbf{u}) - (n_P - 1) \frac{\partial P}{\partial s_l}(\mathbf{u}) \right. \\
& \left. \left. + n_Q(n_Q - 1) u_l Q(\mathbf{u}) - (n_Q - 1) \frac{\partial Q}{\partial s_l}(\mathbf{u}) \right] \right. \\
& + \sqrt{\frac{3}{2}} \frac{1}{|s|} \left\{ -u_l \left[(n_P - 1) \frac{\partial P}{\partial s_k}(\mathbf{u}) + (n_Q - 1) \frac{\partial Q}{\partial s_k}(\mathbf{u}) \right] \right. \\
& \left. + \frac{\partial^2 P}{\partial s_k \partial s_l}(\mathbf{u}) + \frac{\partial^2 Q}{\partial s_k \partial s_l}(\mathbf{u}) \right\}
\end{aligned}$$

which after some rearrangement obtains:

$$\begin{aligned}
& \frac{\partial^2 \hat{f}}{\partial s_k \partial s_l} = \\
& \frac{1}{|s|} \sqrt{\frac{3}{2}} \left\{ \delta_{kl} [1 - (n_P - 1) P(\mathbf{u}) - (n_Q - 1) Q(\mathbf{u})] \right. \\
& + u_k u_l \left[(n_P^2 - 1) P(\mathbf{u}) + (n_Q^2 - 1) Q(\mathbf{u}) - 1 \right] - \\
& (n_P - 1) \left[u_k \frac{\partial P}{\partial s_l}(\mathbf{u}) + u_l \frac{\partial P}{\partial s_k}(\mathbf{u}) \right] - (n_Q - 1) \left[u_k \frac{\partial Q}{\partial s_l}(\mathbf{u}) + u_l \frac{\partial Q}{\partial s_k}(\mathbf{u}) \right] \\
& \left. + \frac{\partial^2 P}{\partial s_k \partial s_l}(\mathbf{u}) + \frac{\partial^2 Q}{\partial s_k \partial s_l}(\mathbf{u}) \right\}
\end{aligned} \quad (123)$$

Similarly to the closing note of Appendix A, we underline here that, despite the use of Voigt's notation (for brevity), the derivatives denoted above by H_{ij} are in fact tensor components.

Appendix C. A note on the r-value equation

In the context of orthotropic symmetry, the description of uniaxial traction/compression tests is usually limited to the $[0^\circ, 90^\circ]$ interval of testing directions (with respect to the rolling direction). Directional properties outside this interval need not be considered, since these are implicitly determined by the assumed symmetry. Nevertheless, our proto-model of the yield surface does require a look at these properties beyond the $[0^\circ, 90^\circ]$ interval and here are discussed the necessary details.

The context here is that of Section 2, with the reference frame e_1 , e_2 and e_3 aligned along the RD, TD and ND (normal to the sheet plane direction), respectively. In the plane of the sheet, the loading direction is specified by

$$\boldsymbol{\nu}(\theta) = (\cos \theta) e_1 + (\sin \theta) e_2, \quad 0 \leq \theta \leq \pi \quad (124)$$

and the stress state generated by a uniaxial test on a sample cut out from the sheet along the direction of $\boldsymbol{\nu}(\theta)$ is

$$\boldsymbol{\sigma}(\theta) = \tau(\theta) \boldsymbol{\nu} \otimes \boldsymbol{\nu} = \tau_\theta \begin{bmatrix} \cos^2 \theta & \sin \theta \cos \theta \\ \sin \theta \cos \theta & \sin^2 \theta \end{bmatrix} \quad (125)$$

where, to avoid confusion in notation, $\tau(\theta)$ denotes the yielding stress along the loading direction; thus either $\tau \equiv \sigma_T$, when the loading is tensile, or $\tau \equiv \sigma_C$, when the loading is a compression. The direction transverse to the loading direction $\boldsymbol{\nu}$ is defined as

$$\boldsymbol{\nu}^\perp = (-\sin \theta) e_1 + (\cos \theta) e_2, \quad 0 \leq \theta \leq \pi \quad (126)$$

being uniquely determined by $\boldsymbol{\nu}^\perp \cdot \boldsymbol{\nu} = 0$ and the requirement that the frame $\{\boldsymbol{\nu}, \boldsymbol{\nu}^\perp\}$ have the same orientation as $\{e_1, e_2\}$. The $r_{T\theta}$ value of the test is defined as the ratio

$$r_{T\theta} = \frac{\epsilon_\perp}{\epsilon_{ND}} = \frac{d\epsilon_\perp}{de_{ND}} \quad (127)$$

where ϵ_\perp and $d\epsilon_\perp$ denote the strain and strain increment along $\boldsymbol{\nu}^\perp$, while ϵ_{ND} and de_{ND} denote the strain and strain increment in the

normal direction. The second equality assumes that the experiments take place at a constant strain rate: $\dot{\epsilon} = const \implies \epsilon(t) = \int_0^t \dot{\epsilon} dt = t\dot{\epsilon}$. Then with

$$d\epsilon_\perp = (d\epsilon : \boldsymbol{\nu}_\perp) \cdot \boldsymbol{\nu}_\perp = (\sin^2 \theta) d\epsilon_{xx} + (\cos^2 \theta) d\epsilon_{yy} - (2 \sin \theta \cos \theta) d\epsilon_{xy} \quad (128)$$

and with (by invoking the incompressibility of the plastic flow and the rigid-plastic approximation)

$$d\epsilon_{ND} = d\epsilon_{zz} = -d\epsilon_{xx} - d\epsilon_{yy} \quad (129)$$

Eq. (127) implies

$$(r_\theta + \sin^2 \theta) d\epsilon_{xx} + (r_\theta + \cos^2 \theta) d\epsilon_{yy} - (2 \sin \theta \cos \theta) d\epsilon_{xy} = 0 \quad (130)$$

In the rigid-plastic approximation there holds

$$d\epsilon = (d\lambda) \frac{\partial f}{\partial \sigma}(\sigma) = (d\lambda) \frac{\partial f}{\partial \sigma}(\gamma)$$

with f the yield function, with $d\lambda > 0$, and with γ denoting any of the four curves in Eqs. (35)–(38) (n.b., without any assumptions on their symmetry about the $\sigma_{xy} = 0$ plane). The second equality holds because f is first order positive homogeneous. Then Eq. (130) rewrites:

$$\begin{aligned}
& (r_\theta + \sin^2 \theta) \frac{\partial f}{\partial \sigma_{xx}}(\gamma) + (r_\theta + \cos^2 \theta) \frac{\partial f}{\partial \sigma_{yy}}(\gamma) \\
& - 2 \sin \theta \cos \theta \frac{\partial f}{\partial \sigma_{xy}}(\gamma) = 0, \quad 0 \leq \theta \leq \pi
\end{aligned} \quad (131)$$

This is the r-value equation in its most general form: with no assumptions on material symmetry.

Finally, we assume orthotropic symmetry and employ an angular parameter θ_{ort} in the interval $[0, \pi/2]$. The above equation remains unchanged when $\gamma \in \{\gamma_T, \gamma_C\}$, because both $\tau(\theta)$ and γ are already parameterized on the interval $[0^\circ, 90^\circ]$. However, when $\gamma \in \{\gamma_T^s, \gamma_C^s\}$, there holds $\theta = \pi/2 + \theta_{ort}$ and $\tau(\theta) = \tau(\pi/2 - \theta_{ort})$ (with a similar relation for the r-value); Then with $\sin(\theta) = \cos(\theta_{ort}) = \sin(\pi/2 - \theta_{ort})$ and $\cos(\theta) = -\sin(\theta_{ort}) = -\cos(\pi/2 - \theta_{ort})$, the r-value equation becomes

$$\begin{aligned}
& (r_{\hat{\theta}} + \sin^2 \hat{\theta}) \frac{\partial f}{\partial \sigma_{xx}}(\gamma^s) \\
& + (r_{\hat{\theta}} + \cos^2 \hat{\theta}) \frac{\partial f}{\partial \sigma_{yy}}(\gamma^s) + 2 \sin \hat{\theta} \cos \hat{\theta} \frac{\partial f}{\partial \sigma_{xy}}(\gamma^s) = 0
\end{aligned} \quad (132)$$

where $\hat{\theta} = \pi/2 - \theta_{ort}$ and γ^s is any of the curves γ_T^s and γ_C^s .

Appendix D. Generating convexity constraints

In this appendix, the procedure for generating the convexity constraints is described. For completeness, the context is general, applicable to 3D stress states. More specific implementation details are discussed for plane stress.

The first essential step consists in generating a set of sampling points distributed uniformly over the unit sphere of the 3D space (s_1, s_2, s_3) for plane stress, or on the unit sphere of the 5D space $(s_1, s_2, s_3, s_4, s_5)$ for general 3D stress states. Generating a set of random points uniformly distributed over the unit hyper-sphere is an easy task when done using a statistical library: one draws a set of n-dimensional tuples with components normally distributed followed by length-normalization. This kind of sampling will be used as an alternative mean of verification of convexity. However, since we require precise control over the locations where some of the convexity constraints are enforced (such as the biaxial curve in the $(\sigma_{xx}, \sigma_{yy})$ plane, or the simple shear points) we adopt a deterministic approach as follows. Considering the 4D unit hyper-sphere parameterized by spherical coordinates⁹ $\theta_1 \in [0, 2\pi)$ and

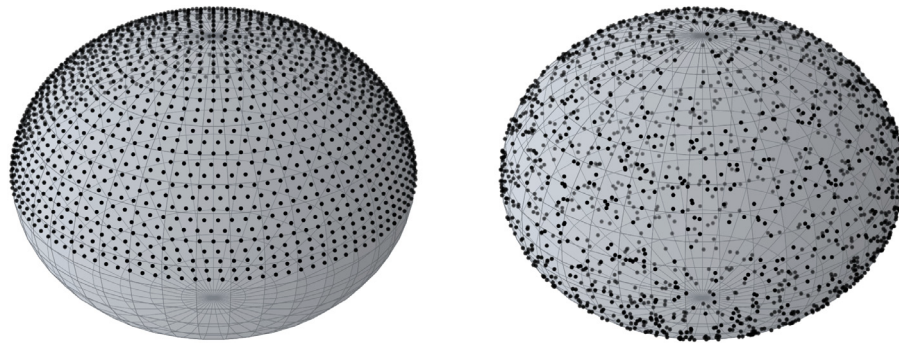


Fig. 26. Uniform sampling of 1,653 and of $2 \times 1,653$ points on the unit sphere of the 3D space: deterministic (on the left) and random (on the right) distributions.

$\theta_2, \theta_3, \theta_4 \in [0, \pi/2]$, we have

$$\left\{ \begin{array}{l} u_5 = \cos \theta_4 \\ u_4 = \sin \theta_4 \cos \theta_3 \\ u_3 = \sin \theta_4 \sin \theta_3 \cos \theta_2 \\ u_2 = \sin \theta_4 \sin \theta_3 \sin \theta_2 \sin \theta_1 \\ u_1 = \sin \theta_4 \sin \theta_3 \sin \theta_2 \cos \theta_1 \end{array} \right. \quad (133)$$

We seek to construct a grid of points on the sphere such that each corresponding coordinate line has the same density of points as a great circle. This condition is chosen because it ensures that the biaxial curve is sampled by a number of uniformly distributed points of our choice. Thus if N (or $N + 1$ when the right-hand extremity 2π is included) is the desired number of points on a great circle, then the spacing interval δ is determined by

$$N\delta = 2\pi \iff \delta = \frac{2\pi}{N}$$

Parameter θ_4 is associated only with great circles and hence its variation interval is sampled by the sequence

$$\left(\theta_4^{(i)} \right)_i = \{ i\delta \mid i = 0, \dots, N_4 \} = \left[\theta_4^{(0)}, \theta_4^{(1)}, \dots, \theta_4^{(N_4-1)}, \theta_4^{(N_4)} \right]$$

with $\theta_4^{(0)} = 0$, $\theta_4^{(N_4)} = \pi/2$ and N_4 determined by¹⁰:

$$N_4\delta = \frac{\pi}{2} \implies N_4 = N/4$$

Next, for each $\theta_4^{(i)}$, the parameter θ_3 is associated with great circles on a sphere in the 4D-space (u_1, u_2, u_3, u_4) of radius $\sin \theta_4^{(i)}$ and hence its variation interval is sampled by the uniform grid

$$\left(\theta_3^{(i,j)} \right)_{i,j} = \{ j\delta \mid j = 0, \dots, N_3(i) \} = \left[\theta_3^{(i,0)}, \theta_3^{(i,1)}, \dots, \theta_3^{(i,N_3(i))} \right]$$

with $N_3(i)$ determined by

$$N_3(i)\delta = \frac{\pi}{2} \sin \theta_4^{(i)} \implies N_3(i) = \frac{N}{4} \sin \theta_4^{(i)}$$

Next, for each $\theta_4^{(i)}$ and $\theta_3^{(i,j)}$, parameter θ_2 is associated with great circles on a sphere in the 3D-space (u_1, u_2, u_3) of radius $\sin \theta_4^{(i)} \sin \theta_3^{(i,j)}$ and hence its variation interval is sampled by the uniform grid

$$\left(\theta_2^{(i,j,k)} \right)_{i,j,k} = \{ k\delta \mid k = 0, \dots, N_2(i, j) \} = \left[\theta_2^{(i,j,0)}, \theta_2^{(i,j,1)}, \dots, \theta_2^{(i,j,N_2(i,j))} \right]$$

with $N_2(i, j)$ determined by

$$N_2(i, j)\delta = \frac{\pi}{2} \sin \theta_4^{(i)} \sin \theta_3^{(i,j)} \implies N_2(i, j) = \frac{N}{4} \sin \theta_4^{(i)} \sin \theta_3^{(i,j)}$$

⁹ Because of the general context of orthotropic symmetry, only half of the sphere need be sampled and hence the half intervals for θ_2 , θ_3 , and θ_4 .

¹⁰ In code, the formula is actually implemented as $N_4 = \text{integer}(N/4)$ and similarly for N_3 , N_2 and N_1 below.

Finally, for each $\theta_4^{(i)}$, $\theta_3^{(i,j)}$, and $\theta_2^{(i,j,k)}$, parameter θ_1 describes a full circle of radius $\sin \theta_4^{(i)} \sin \theta_3^{(i,j)} \sin \theta_2^{(i,j,k)}$ and hence its variation interval is sampled by the uniform grid

$$\begin{aligned} \left(\theta_1^{(i,j,k,m)} \right)_{i,j,k,m} &= \{ m\delta \mid m = 0, \dots, N_1(i, j, k) \} \\ &= \left[\theta_1^{(i,j,k,0)}, \theta_1^{(i,j,k,1)}, \dots, \theta_1^{(i,j,k,N_1(i,j,k))} \right] \end{aligned}$$

with $N_1(i, j, k)$ determined by

$$\begin{aligned} N_1(i, j, k)\delta &= 2\pi \sin \theta_4^{(i)} \sin \theta_3^{(i,j)} \sin \theta_2^{(i,j,k)} \\ &\implies N_1(i, j, k) = N \sin \theta_4^{(i)} \sin \theta_3^{(i,j)} \sin \theta_2^{(i,j,k)} \end{aligned}$$

With $N = 100$, corresponding to 101 sampling locations on the equator, the above procedure generates on the 4D unit sphere of the 5D space a total of 233,127 points. By comparison, the brute force approach, where $[0, 2\pi] \times [0, \pi/2]^3$ is sampled directly by a uniform grid, generates $100 \times 25^3 = 1,562,500$ points: besides generating almost 7 times more points than the above procedure, a large fraction of these is concentrated near the top of the sphere, which would render many of the corresponding constraints practically redundant (because of the continuity of the hessian).

The plane stress case is obtained similarly or directly from the above formulas where $\theta_4 = \pi/2$, $\theta_3 = \pi/2$, $N_2 = N/4$ and $N_1 = N \sin \theta_2$. With $N = 100$ one obtains 1,653 points uniformly distributed on the 2D unit sphere of the 3D space as illustrated in Fig. 26. The same figure shows also an equivalent random distribution.

At each sampling location, denoted, generically, by \mathbf{u}_S , not located at one of the north poles $\theta_i = 0$, $i = 2, 3, 4$, the tangent space is generated by the four vectors tangent to the coordinates lines

$$\mathbf{v}_k(\mathbf{u}_S) = \frac{\partial \mathbf{u}}{\partial \theta_k} = \frac{\partial \mathbf{u}_i}{\partial \theta_k} \mathbf{e}_i \quad (134)$$

where $\{\mathbf{e}_i\}$ is the canonical orthonormal frame of \mathbb{S} , with \mathbf{e}_5 pointing to the north pole $\theta_4 = 0$. A discrete set of unit tangent vectors is then generated by

$$V(\mathbf{u}_S) = \{ \mathbf{t} = \mathbf{v}/|\mathbf{v}| \mid \mathbf{v} = \lambda_1 \mathbf{v}_1 + \lambda_2 \mathbf{v}_2 + \lambda_3 \mathbf{v}_3 + \lambda_4 \mathbf{v}_4 \}$$

and the convexity condition (65) is enforced at \mathbf{u}_S in the form:

$$[\widehat{H}(\mathbf{u}_S) : \mathbf{t}] \cdot \mathbf{t} \geq \epsilon, \quad \forall \mathbf{t} \in V(\mathbf{u}_S) \quad (135)$$

with $\epsilon > 0$ a small number.

The north poles of the spherical coordinate system are singular points (the Jacobian of the map in Eq. (133) vanishes). Nevertheless, it is easy to see that the following sets of vectors are linearly independent and tangent, and hence can be used to generate the set V .

- When $\theta_4 = 0$: $\{\mathbf{e}_1, \mathbf{e}_2, \mathbf{e}_3, \mathbf{e}_4\}$
- When $\theta_4 > 0, \theta_3 = 0$: $\{\mathbf{e}_1, \mathbf{e}_2, \mathbf{e}_3, \mathbf{v}_4\}$
- When $\theta_4 > 0, \theta_3 > 0, \theta_2 = 0$: $\{\mathbf{e}_1, \mathbf{e}_2, \mathbf{v}_3, \mathbf{v}_4\}$

For the case of plane stress, the set V reduces to

$$V = V(\mathbf{u}_S) = \{t = \mathbf{v}/|\mathbf{v}| \mid \mathbf{v} = \lambda_1 \mathbf{v}_1 + \lambda_2 \mathbf{v}_2\}$$

In the actual numerical implementation we used a set of 51 such tangent vectors at each point where convexity is enforced. Using Eqs. (60) and (65), Eq. (135) reduces to

$$\begin{aligned} & (n_P - 1)P - (H_{P11}t_1^2 + H_{P22}t_2^2 + H_{P33}t_3^2 + 2H_{P12}t_1t_2 \\ & + 2H_{P13}t_1t_3 + 2H_{P23}t_2t_3) + \\ & (n_Q - 1)Q - (H_{Q11}t_1^2 + H_{Q22}t_2^2 + H_{Q33}t_3^2 \\ & + 2H_{Q12}t_1t_2 + 2H_{Q13}t_1t_3 + 2H_{Q23}t_2t_3) \leq 1 - \epsilon \end{aligned} \quad (136)$$

where $t = (t_1, t_2, t_3)$. The above expression was expanded deliberately into its P -part and Q -part to highlight that its structure is similar to that of Eq. (17); Hence the procedure followed for implementing a constraint: each term is a sum of monomials, each monomial has a unique corresponding material parameter.

Finally, after a set of parameters has been identified, the convexity of the resulting SHYqp function is verified by calculating the leading principal minors of $\bar{\mathbf{H}}$ and the Gaussian curvature K on a dense set of random locations as in Fig. 26/Right. The Gaussian curvature is calculated by the formula, Goldman (2005):

$$K = \frac{1}{|Df|^4} (\mathbf{H}^* : Df) \cdot Df \quad (137)$$

Note that Df and \mathbf{H} are the gradient and hessian of the function $f = f(\sigma)$. Also, \mathbf{H}^* is the cofactor matrix of \mathbf{H} , i.e., $H_{ij}^* = (-1)^{i+j} \det(M_{ij})$, where M_{ij} is the 2×2 matrix obtained from \mathbf{H} by eliminating row i and column j .

Appendix E. Tables of mechanical properties

For the convenience of the reader, this appendix lists the experimental data used for the models illustrated in Section 7. In all tables, angles are measured from the rolling direction and stress units are in MPa (where raw stress data was reported numerically); The column $\sigma_{xx} = \sigma_{yy}$ records the balanced-biaxial experiment; Missing values are indicated by ‘*’.

Table 3

Mechanical data reported in Lou et al. (2007) for magnesium sheet AZ31B.

Type	Data	0°	45°	90°	$\sigma_{xx} = \sigma_{yy}$
Tension	σ	164	180	192	*
	r-val	1.7	2.6	4.3	*
Compression	σ	104	105	110	*
	r-val	0.2	0.25	0.4	*

Table 4

Mechanical data reported in Andar et al. (2012) for magnesium sheet AZ31B.

Type	Data	0°	45°	90°	$\sigma_{xx} = \sigma_{yy}$
Tension	σ	198	204	212	186
	r-val	2.56	3.66	3.35	*
Compression	σ	158	*	157	*
	r-val	0.14	*	0.16	*

Table 5

Mechanical data reported in Raemy et al. (2017) for Ti-CP Grade 4 alloy. Note: the cited reference mentions that the r-values in compression could not be measured experimentally and assumed these to be equal to the corresponding values in tension.

Type	Data	0°	45°	90°	$\sigma_{xx} = \sigma_{yy}$
Tension	σ	569	620	651	800
	r-val	1.05	2.10	2.25	*
Compression	σ	751	600	580	606
	r-val	1.05	2.10	2.25	*

Table 6

Mechanical data reported in Anon (2011), p.229, for aluminum alloy AA5042-H2.

Type	Data	0°	15°	30°	45°
Tension	σ	277.17	277.17	282.00	281.31
	r-val	0.3540	0.2390	0.6400	1.0690
		60°	75°	90°	$\sigma_{xx} = \sigma_{yy}$
	σ	282.00	287.51	289.58	296.99
	r-val	1.2790	1.2240	1.3960	0.9910

Table 7

Mechanical data reported in Aretz and Barlat (2004) for aluminum alloy AA2090-T3.

Note: stress data is normalized in the cited reference.

Type	Data	0°	15°	30°	45°
Tension	σ	1.0000	0.9605	0.9102	0.8114
	r-val	0.2115	0.3269	0.6923	1.5769
		60°	75°	90°	$\sigma_{xx} = \sigma_{yy}$
	σ	0.8096	0.8815	0.9102	1.0350
	r-val	1.0385	0.5384	0.6923	0.6700

Table 8

Mechanical data extracted from data reported in Li et al. (2020) for the dual phase AHSS steel DP980.

Type	Data	0°	15°	30°	45°
Tension	σ	684.76	699.90	698.89	691.84
	r-val	0.7514	0.7912	0.8781	0.8632
		60°	75°	90°	$\sigma_{xx} = \sigma_{yy}$
	σ	710.18	708.84	712.23	*
	r-val	0.8719	0.8046	0.7614	*

References

- Agnew, R.R., Duygulu, O., 2005. Plastic anisotropy and the role of non-basal slip in magnesium alloy AZ31B. *Int. J. Plast.* 21, 1161–1193.
- Andar, M.O., Kuwabara, T., Steglich, D., 2012. Material modeling of AZ31 Mg sheet considering variation of r-values and asymmetry of the yield locus. *Mater. Sci. Eng. A* 549, 82–92.
- Anon, 2011. In: Huh, H., Chung, K., Han, S.S., Chung, W.J. (Eds.), Proc. NUMISHEET 2011 Benchmark Problems and Results.
- Aretz, H., Barlat, F., 2004. General orthotropic yield functions based on linear stress deviator transformations. In: Ghosh, S., Lee, J.K., Castro, J.C. (Eds.), Proc. NUMIFORM 2004 Conference. In: AIP Conf. Proc., vol. 712, pp. 147–156, 2004.
- Bomarito, G.S., Townsend, T.S., Stewart, K.M., Esham, K.V., Emery, J.M., Hochhalter, J.D., 2021. Development of interpretable, data-driven plasticity models with symbolic regression. *Comput. Struct.* 252, 106557.
- Bonet, J., Wood, R.D., 1997. Nonlinear Continuum Mechanics for Finite Element Analysis. Cambridge University Press, (Chapter 7).
- Boyd, S., Vandenberghe, L., 2004. Convex Optimization. Cambridge University Press, (Python code at, <https://cvxopt.org/>).
- Eggersmann, R., Kirchdoerfer, T., Reese, S., Stainier, L., Ortiz, M., 2019. Model-free data-driven inelasticity. *Comput. Methods Appl. Mech. Engrg.* 350, 81–89.
- Esmaili, A., Asadi, S., Larsson, F., Runesson, K., 2019. Construction of macroscale yield surfaces for ductile composites based on a virtual testing strategy. *Eur. J. Mech. -A/Solids* 77, 103786.
- Fuhg, J.N., Fau, A., Bouklas, N., Marino, M., 2022. Elasto-plasticity with convex model-data-driven yield functions. Preprint.
- Goldfarb, D., Idnani, A., 1983. A numerically stable dual method for solving strictly convex quadratic programs. *Math. Program.* 27, 1–33, (Python code at: <https://pypi.org/project/quadprog/> or at: <https://github.com/quadprog/quadprog>).
- Goldman, R., 2005. Curvature formulas for implicit curves and surfaces. *Comput. Aided Geom. Design* 22, 632–658.
- Graf, S., Brocks, W., Steglich, D., 2007. Yielding of magnesium: From single crystal to polycrystalline aggregates. *Int. J. Plast.* 23, 1957–1978.
- Groemer, H., 1996. Geometric Applications of Fourier Series and Spherical Harmonics. Cambridge University Press.
- Hao, S., Dong, X., 2020. Interpolation-based plane stress anisotropic yield models. *Int. J. Mech. Sci.* 178, 105612.
- Hershey, A.V., 1954. The plasticity of anisotropic aggregate of anisotropic face centered cubic crystals. *J. Appl. Mech.* 21, 241–249.
- Hill, R., Hutchinson, J.W., 1992. Differential hardening in sheet metal under biaxial loading: A theoretical framework. *J. Appl. Mech.* 59 (2S), S1–S9.

- Hosford, W.F., 1972. A generalized isotropic yield criterion. *J. Appl. Mech.* 39, 607–609.
- Ibanez, R., Chavanne, E.A., Aguado, J.V., Gonzalez, D., Cueto, E., Chinesta, F., 2016. A manifold learning approach to data-driven computational elasticity and inelasticity. *Arch. Comput. Methods Eng.* 25, 47–57.
- Kondori, B., Madi, Y., Besson, J., Benzerga, A.A., 2019. Evolution of the 3D plastic anisotropy of HCP metals: Experiments and modeling. *Int. J. Plast.* 117, 71–92.
- Kraska, M., Doig, M., Tikhomirov, D., Raabe, D., Roters, F., 2009. Virtual material testing for stamping simulations based on polycrystal plasticity. *Comput. Mater. Sci.* 46, 383–392.
- Li, Q., Zhang, H., Chen, F., Xu, D., Sui, D., Cui, Z., 2020. Study on the plastic anisotropy of advanced high strength steel sheet: Experiments and microstructure-based crystal plasticity modeling. *Int. J. Mech. Sci.* 176, 105569.
- Lou, X.Y., Li, M., Boger, R.K., Agnew, S.R., Wagoner, R.H., 2007. Hardening evolution of AZ31b Mg sheet. *Int. J. Plast.* 23, 44–86.
- Palaniswamy, H., Al-Nasser, A., 2012. Forming of advanced high-strength steels (AHSS). In: Altan, T., Tekkaya, E. (Eds.), *Sheet Metal Forming - Processes and Applications*. ASM International, Materials Park, Ohio.
- Plunkett, B., Cazacu, O., Barlat, F., 2008. Orthotropic yield criteria for description of the anisotropy in tension and compression of sheet metals. *Int. J. Plast.* 24, 847–866.
- Raemy, C., Manopulo, N., Hora, P., 2017. On the modelling of plastic anisotropy, asymmetry and directional hardening of commercially pure titanium: A planar Fourier series based approach. *Int. J. Plast.* 91, 182–204.
- Roters, F., Diehl, M., Eisenlohr, P., Shanthraj, P., Reuber, C., Wong, S.L., Maiti, T., Ebrahimi, A., Hochrainer, T., Fabritius, H.-O., Nikolov, S., Friák, M., Fujita, N., Grilli, N., Janssens, K.G.F., Jia, N., Kok, P.J.J., Ma, D., Meier, F., Werner, E., Stricker, M., Weygand, D., Raabe, D., 2019. DAMASK – the Düsseldorf advanced material simulation kit for modeling multi-physics crystal plasticity, thermal, and damage phenomena from the single crystal up to the component scale. *Comput. Mater. Sci.* 158, 420–478, (Web: <https://damask.mpie.de/>).
- Seifert, T., Schmidt, I., 2008. Line-search methods in general return mapping algorithms with application to porous plasticity. *Int. J. Num. Methods Eng.* 73, 1468–1495.
- Soare, S.C., 2022. A parameter identification scheme for the orthotropic Poly6 yield function satisfying the convexity condition. *Eur. J. Mech. - A/Solids* 92, 104467.
- Soare, S.C., Barlat, F., 2011. A study of the Yld2004 yield function and one extension in polynomial form: A new implementation algorithm, modeling range, and earing predictions for aluminum alloy sheets. *Eur. J. Mech. - A/Solids* 30, 807–819.
- Soare, S.C., Barlat, F., 2014. About the influence of hydrostatic pressure on the yielding and flow of metallic polycrystals. *J. Mech. Phys. Solids* 67, 87–99.
- Soare, S.C., Benzerga, A.A., 2016. On the modeling of asymmetric yield functions. *Int. J. Solids Struct.* 80, 486–500.
- Spitzig, W.A., Richmond, O., 1984. The effect of pressure on the flow stress of metals. *Acta Metall.* 32, 457–463.
- Steglich, D., Tian, X., Besson, J., 2016. Mechanism-based modelling of plastic deformation in magnesium alloys. *Eur. J. Mech. - A/Solids* 55, 289–303.
- Tong, W., 2018. Calibration of a complete homogeneous polynomial yield function of six degrees for modeling orthotropic steel sheets. *Acta Mech.* 229, 2495–2519.
- Vegter, H., Boogaard, A.H., 2006. A plane stress yield function for anisotropic sheet material by interpolation of biaxial stress states. *Int. J. Plast.* 22, 557–580.
- Vegter, H., Drent, P., Huetink, J., 1995. A planar isotropic yield criterion based on mechanical testing at multi-axial stress states. In: Shen, S.-F., Dawson, P.R. (Eds.), *Simulation of Materials Processing: Theory, Methods and Applications*. Balkema, Rotterdam, pp. 345–350.
- Vlassis, N.N., Sun, W.C., 2021. Sobolev training of thermodynamic-informed neural networks for interpretable elasto-plasticity models with level set hardening. *Comput. Methods Appl. Mech. Engrg.* 377, 113695.
- Wang, Y., Wagner, N., Rondinelli, J.M., 2019. Symbolic regression in materials science. *MRS Commun.* 9, 793–805.
- Yoon, J., Cazacu, O., Mishra, R.K., 2013. Constitutive modeling of AZ31 sheet alloy with application to axial crushing. *Mater. Sci. Eng. A* 565, 203–212.
- Yoon, J.W., Lou, Y., Yoon, J., Glazoff, M.V., 2014. Asymmetric yield function based on the stress invariants for pressure sensitive metals. *Int. J. Plast.* 56, 184–202.
- Zecevic, M., Beyerlein, I.J., Knezevic, M., 2018. Activity of pyramidal I and II <+a>slip in Mg alloys as revealed by texture development. *J. Mech. Phys. Solids* 111, 290–307.
- Zhang, K., Holmedal, B., Hopperstad, O.S., Dumoulin, S., Gawad, J., Van Bael, A., Van Houtte, P., 2015. Multi-level modelling of mechanical anisotropy of commercial pure aluminium plate: crystal plasticity models, advanced yield functions and parameter identification. *Int. J. Plast.* 66, 3–30.